J. Fluid Mech. (1999), *vol.* 387, *pp.* 3–37. Printed in the United Kingdom

High-order structure functions of turbulence

By WILLEM VAN DE WATER
AND JANINE A. HERWEIJER

Physics Department, Eindhoven University of Technology, P.O. Box 513,
5600 MB, Eindhoven, The Netherlands

(Received 14 March 1996 and in revised form 20 October 1998)

The scaling behaviour of high-order structure functions $G_p(r) = \langle (\boldsymbol{u}(\boldsymbol{x}+\boldsymbol{r}) - \boldsymbol{u}(\boldsymbol{x}))^p \rangle$ is studied in a variety of laboratory turbulent flows. The statistical accuracy of the structure function benefits from novel instrumentation for its real-time measurement. The nature of statistical errors is discussed extensively. It is argued that integration times must increase for decreasing separations r. Based on the statistical properties of probability density functions we derive a simple estimate of the required integration time for moments of a given order. We further give a way for improving this accuracy through careful extrapolation of probability density functions of velocity differences.

Structure functions are studied in two different kinematical situations. The (standard) longitudinal structure functions are measured using Taylor's hypothesis. In the transverse case an array of probes is used and no recourse to Taylor's hypothesis is needed. The measured scaling exponents deviate from Kolmogorov's (1941) prediction, more strongly so for the transverse exponents.

The experimental results are discussed in the light of the multifractal model that explains intermittency in a geometrical framework. We discuss a prediction of this model for the form of the structure function at scales where viscosity becomes of importance.

1. Introduction

About 15 years ago a paper was published in this Journal in which a careful study was made of high-order structure functions in turbulence (Anselmet *et al.* 1984). The structure function is defined as

$$G_p(r) = \langle (\Delta u(r))^p \rangle, \tag{1.1}$$

where the velocity difference $\Delta u(r)$ is measured over a distance r, $\Delta u(r) = u(x+r) - u(x)$ and the average is done over x (which is interpreted as an ensemble average). According to Kolmogorov (1941), the structure function has scaling behaviour

$$G_p(r) \sim r^{\zeta(p)}. \tag{1.2}$$

The possible existence of *universal* scaling exponents $\zeta(p)$ is one of the most exciting aspects of turbulence. Anselmet *et al.* (1984) verified that the scaling exponent $\zeta(p)$ differed significantly from Kolmogorov's similarity prediction $\zeta(p) = p/3$. This has spawned considerable theoretical and experimental activity in the past years, an extensive historical account of which has been given by Frisch (1995). Using scaling concepts from the physical theory of critical phenomena a new model for this 'anomalous' (that is deviant from self-similar) behaviour of the function $\zeta(p)$ was described by Mandelbrot (1974) and by Parisi & Frisch (1985). It was carried over

to the statistical description of chaotic motion in low-dimensional dynamical systems by Benzi *et al.* (1984) and Halsey *et al.* (1986).

Similar scaling properties could be found for the dissipation field $\epsilon(\boldsymbol{r})$ (Sreenivasan & Meneveau 1988; Chhabra *et al.* 1989; Meneveau & Sreenivasan 1991). Whereas ϵ is a *dissipation-range* quantity, the scaling of the velocity increments $\Delta u(r)$ is a property of the *inertial-range* statistics of turbulence. The relation between these two points of view is the subject of the refined similarity hypothesis by Kolmogorov (1962).

In the present paper we will report on laboratory experiments in turbulent air flows. These experiments concern a precise measurement of the scaling exponent $\zeta(p)$ for both longitudinal and transverse velocity differences and the precise form of the structure function $G_p(r)$. In all our experiments the measured component of $\boldsymbol{u}$ points in the direction of the mean flow. Structure functions can be measured for the case that $\boldsymbol{r}$ is parallel to $\boldsymbol{u}$ (longitudinal structure functions $G_p^L(r)$) and for the case that $\boldsymbol{r}$ is perpendicular to $\boldsymbol{u}$ (transverse structure functions $G_p^T(r)$). Let us call $\zeta^L(p)$ and $\zeta^T(p)$ the associated scaling exponents. On the basis of scaling arguments alone, one would expect $\zeta^L(p)$ and $\zeta^T(p)$ to be the same. A point of concern of this paper, however, is the possible existence of differences between these two exponents.

Transverse structure functions with $\boldsymbol{r}$ parallel to the mean flow direction (and thus $\boldsymbol{u}$ perpendicular to $\boldsymbol{U}$) have been measured by Saddoughi & Veeravalli (1994) who show results for G_2, G_3 and power spectra, and by Camussi *et al.* (1996) who concentrate on relative scaling properties of high-order moments. The experimental assessment of isotropy is the main point of Saddoughi & Veeravalli (1994) who give an excellent review of earlier work on this problem. Transverse structure functions with $\boldsymbol{r}$ perpendicular to the mean flow direction were measured by Noullez *et al.* (1997) using a novel laser-spectroscopic technique. The information contained in these structure functions is comparable to that obtained by us, but the optical method used by them allows resolution of much smaller scales.

The average in (1.1) can be trivially written as an integral over the probability density function $P_r(\Delta u)$ of velocity differences Δu that are measured a distance r apart. Thus, the structure function $G_p(r)$ is the pth moment of the probability density function $P_r(\Delta u)$ of velocity differences $\Delta u(r)$. The probability density function (PDF) $P_r^L(\Delta u)$ of longitudinal velocity differences is skewed, whereas the PDF of transverse Δu, $P_r^T(\Delta u)$, is symmetric. The skewness of the longitudinal PDF is connected with the spectral energy cascade and underlies the existence of the odd-order moments. The difference between longitudinal and transverse PDFs can be understood on basis of a simple symmetry argument. In the longitudinal configuration the possibility of conveying information from the point $\boldsymbol{x}$ to the point $\boldsymbol{x}+\boldsymbol{r}$ depends on the sign of the velocity difference $\Delta\boldsymbol{u}$; hence the asymmetry of the PDF. In the transverse case with the velocities $\boldsymbol{u}(\boldsymbol{x})$ and $\boldsymbol{u}(\boldsymbol{x}+\boldsymbol{r})$ perpendicular to $\boldsymbol{r}$, no such asymmetry can exist for homogeneous turbulence.

The probability density functions (and not just their moments) may also have scaling properties. A comparison to intermittency models has been reported by Castaing, Gagne & Hopfinger (1990), Chabaud *et al.* (1994) and Benzi *et al.* (1991). Because the statistical accuracy of high-order moments is problematic, it may be advantageous to directly work with the PDFs rather than with their moments.

In § 2 we describe the theoretical framework of our experiments. A brief introduction to intermittency models is given but we concentrate on the multifractal model by Parisi & Frisch (1985). For discriminating intermittency models and for testing further consequences it is of key importance to know the scaling exponents $\zeta(p)$ for large values of p and the precise form of the structure functions $G_p(r)$. The statistical

accuracy of high-order moments is a difficult problem because they are determined by the increasingly rare instances of increasingly violent turbulent events.

A central point of our experimental work has been the design of novel turbulence instrumentation that allows the real-time processing of extremely large data sets. The flow configuration used is discussed in § 3.1 and the instrumentation is detailed in § 3.2. Another key aspect of our experiments is the simultaneous measurement of longitudinal and transverse structure functions using multi-probe arrays.

Results on probability density functions (PDFs) are given in § 4 where we compare the longitudinal and transverse PDFs and point to a surprising coincidence of the negative velocity tails of these PDFs. We confront our data with an intermittency model for the PDF. Whilst the statistical accuracy of high-order moments rapidly diminishes with increasing order, we derive estimates in § 5, both of this accuracy and of the highest moment that can be measured reliably. These estimates are based either on the correlation structure of moments or on the statistical accuracy of measured PDFs.

The use of stretched exponentials to represent the low-probability tails of PDFs is studied in § 6. This is a purely phenomenological approach and the correctness of this representation is assessed using statistical tests. This representation is used to improve the statistical accuracy of high-order moments.

Measured longitudinal and transverse structure functions are discussed in § 7. Of prime interest is the value of the scaling exponents $\zeta(p)$, but we also emphasize the precise form of the structure function $G_p^L(r)$. We show that the residual of $G_p^L(r)$ after dividing out the scaling $r^{\zeta^L(p)}$ has an interesting dependence on p. The transverse experiments were restricted to grid turbulence. It turns out that the deviation of $\zeta^T(p)$ from Kolmogorov's prediction is larger than that of $\zeta^L(p)$. In § 8 we formulate several speculations about this result.

2. Intermittency models

In the past few years, models of the small-scale structure of turbulence have been widely discussed in the literature. From those we have chosen to describe in some depth the multifractal model by Parisi & Frisch (1985). Although this paper's main emphasis is on experimental results, confrontation with the predictions of this particular model leads to valuable new insights. First, however, we will briefly recall two exact results.

One of the few exact results of the statistical theory of turbulence is the Kolmogorov–Kármán–Howarth equation that expresses a relation between the third- and second-order longitudinal structure functions (Monin & Yaglom 1975)

$$G_3(r) = -\tfrac{4}{5}\epsilon r + 6\nu \frac{\mathrm{d}G_2(r)}{\mathrm{d}r}. \tag{2.1}$$

At scales r much larger than the Kolmogorov scale η, but much smaller than an external length scale L, (2.1) predicts that $G_3(r) = -\frac{4}{5}\epsilon r$. An equivalent relation is $G_3(r)/v_k^3 = -\frac{4}{5}r/\eta$, where velocities are non-dimensionalized by the Kolmogorov velocity v_k and length scales by the Kolmogorov length η.

Equation (2.1) applies to the case of stationary, homogenous, and isotropic turbulence. This is a situation that is difficult to realize in the laboratory. In most laboratory experiments, the turbulence is not stationary (in space) as it is, for example, driven by shear or decaying behind a grid. In these cases an extra term that involves the forcing must be added to the right-hand side of (2.1). Yakhot (1995) has argued

that the presence of this term causes an asymmetry between odd and even structure functions. This asymmetry has the result that in the inertial range $G_2(r)$ cannot be written as $[G_3(r)]^{\zeta(2)}$, even when $\zeta(3)$ is precisely one. As a consequence, the even structure functions are not simply rescaled versions of the odd-order ones and the exponents that are determined from the approximate scaling of $G_p(r)$ for even and odd p do not fall on a smooth curve. Vassilicos (1992) pointed out that such asymmetry would be consistent with a multispiral nature of small-scale turbulence and a general multifractal framework for even/odd asymmetry has been given by Vainshtein & Sreenivasan (1994).

For the comparison of longitudinal and transverse structure functions it is useful to recall another exact relation

$$G_2^T(r) = G_2^L(r) + \frac{r}{2}\frac{\mathrm{d}G_2^L(r)}{\mathrm{d}r}, \tag{2.2}$$

that can be derived assuming isotropy and incompressibility. Similar relations can be derived for higher-order structure functions, but they do not seem to be useful because increasingly complicated correlations between transverse and longitudinal velocity differences are involved. Therefore, the statistical properties of longitudinal and transverse velocity differences are not related in a trivial way. Equation (2.2) allows a precise test of isotropy using measured longitudinal second-order longitudinal and transverse structure functions.

The prediction by Kolmogorov (1941) for the scaling exponents $\zeta(p)$, $\zeta(p) = p/3$, implies that the energy dissipation is constant. The log-normal model allows for fluctuations of the local average ϵ_r of the dissipation over intervals of size r (Kolmogorov 1962). Specifically, it assumes that the distribution of $\log \epsilon_r$ is a Gaussian whose width σ depends on r as $\sigma = \mu \log r$, where $\mu = 2 - \zeta(6)$ is the adjustable parameter of the log-normal model. The scaling exponent for the moments of velocity differences then is

$$\zeta(p) = \frac{p}{3} - \tfrac{1}{18}\mu p(p-3). \tag{2.3}$$

The log-normal model predicts a maximum of the exponent $\zeta(p)$ at $p = \frac{1}{2}(6/\mu + 3)$. Currently accepted values of μ are $\mu \approx 0.2$, in which case the maximum would be reached at $p \approx 16$. It is a challenge to measure structure functions that are still statistically meaningful at these large orders.

The log-normal model involves fluctuations of the dissipation rate ϵ_r, a viscous range quantity. It leads to a prediction for the statistics of velocity increments, an inertial range quantity, because fluctuations of $\Delta u(r)$ and ϵ_r are related. This relation is the subject of Kolmogorov's refined similarity hypothesis that has been verified experimentally by Stolovitzky, Kailasnath & Sreenivasan (1992).

2.1. *The multifractal model*

The multifractal model is an attempt to capture intermittency in a geometric framework. It assumes that velocity differences locally scale as $\Delta u(r) \sim r^h$. The exponents h are all $h < 1$, and imply that derivatives of the velocity field are singular. Therefore we will refer to h as the singularity strength. The turbulent fluctuation field consists of a whole range of singularities whose strengths at scale r have a probability that is proportional to $r^{3-\mathrm{D}(h)}$. The function $D(h)$ can be interpreted as the fractal dimension of the set of singularities with strength h. In three dimensions $r^{3-\mathrm{D}(h)}$ is the fraction of space occupied by those exponents. Ensemble averages are now thought of as averages over the distribution of singularities. Notably, for the moments of velocity

increments

$$G_p(r) \sim \int_0^{h_{\max}} r^{ph}\, r^{3-\mathrm{D}(h)}\, \mathrm{d}h. \tag{2.4}$$

In the limit $r \to 0$ this equation singles out a particular exponent $\tilde{h}$, and a steepest descent argument gives

$$\zeta(p) = 3 - D(\tilde{h}) + p\tilde{h}, \text{ where } \tilde{h} \text{ is defined by } \left.\frac{\mathrm{d}D(h)}{\mathrm{d}h}\right|_{h=\tilde{h}} = p. \tag{2.5}$$

Equation (2.5) illustrates that the scaling exponent $\zeta(p)$ and the dimension function $D(h)$ are two complementary ways to describe the small-scale structure of turbulence. The function $D(h)$ is convex. Therefore, the smallest values of h, which are the strongest singularities, correspond to the largest values of p, the highest-order moments. Asymptotically, the highest-order moments are determined by the strongest singularity that can be detected.

The multifractal model *per se* does not provide an explanation for the scaling exponent $\zeta(p)$, other than its association with a geometric property (the dimension $D(h)$) of the small-scale velocity field. In order to arrive at a direct comparision with experimental $\zeta(p)$, several models for $D(h)$ have been proposed. One of these models is the random beta model which owes its name to the random positive numbers β_i from which a random multiplicative process is built for velocity differences $v_n(r_n)$ at level n of a cascade, $v_n = v_0 r_n^{1/3} (\beta_1 \beta_2 \cdots \beta_n)^{1/3}$ (Benzi *et al.* 1984). It is assumed that the random numbers β_i and β_{i+1} are uncorrelated and distributed according to a function $F(\beta)$ which is taken to be of bimodal form $F(\beta) = q\delta(\beta - 1) + (1 - q)\delta(\beta - 1/2)$. Therefore, the breakdown to smaller scales in a binary cascade would be either space-filling ($\beta = 1$) or confined to planes ($\beta = 1/2$). The associated probabilities are q and $1 - q$, respectively. The scaling exponent $\zeta(p)$ and its companion dimension spectrum $D(h)$ follow from $F(\beta)$ in a straightforward manner. It was found that experimental results are reproduced well by selecting the single adjustable parameter q to be $q = 0.875$. Another quite similar single-parameter model is the p-model by Meneveau & Sreenivasan (1987). Narrowing the distribution $F(\beta)$ to a single β leads to the Beta-model by Frisch (1995) which predicts a scaling exponent that depends linearly on p, $\zeta(p) = 3 - D + p(D - 2)/3$.

Quite recently She & Leveque (1994) have proposed a model that does not appeal to adjustable parameters and rests on the assumption of filamentary structures as carriers of the strongest singularities and a space-filling field that carries the mean dissipation. A further assumption concerns the way intermediate singularity structures can be interpolated between these two extremes. This assumption is formulated in terms of moments n of the fluctuating dissipation and was tested experimentally for small n ($n = 3.7$) by Chavarria, Baudet & Ciliberto (1995).

In the past few years there have been several attempts to extend scaling arguments into the intermediate viscous range $r \lesssim 20\eta$. In laboratory experiments, the inertial range where the scaling $G_p(r) \sim r^{\zeta(p)}$ can be observed is often small and extension of scaling theories to smaller distances is extremely useful as it gives a larger range of scales from which a scaling exponent can be determined. Attempts in this direction have been reported by Sirovich, Smith & Yakhot (1994) and Stolovitzky, Sreenivasan & Juneja (1993). Universally valid small-r approximations to $G_p(r)$ may point to interesting physics in the crossover from inertial to viscous dynamics.

Based on phenomenological arguments, Benzi *et al.* (1993) have proposed a

parametrization of $G_p(r)$, as $G_p(r) = \left(f_p(r)r\right)^{\zeta(p)}$. The function $f_p(r)$ models deviations from ideal scaling behaviour. From experimental data it appears that the function $f_{2p}(r)$ has a very weak dependence on $p = 1, 2, \ldots$. Similarly, the function $f_{2p+1}(r)$ has a very weak dependence on p. However, it is found that there is an appreciable difference between $f_{2p}(r)$ and $f_{2p+1}(r)$ for even- and odd-order moments. As is well known, the statistical accuracy of odd-order longitudinal moments is inferior to that of even-order moments. This has led Benzi *et al.* (1993) to compute the odd-order moments from the absolute value of velocity differences $|\Delta u(r)|$. Of course, in this case the asymmetry between $f_{2p}(r)$ and $f_{2p+1}(r)$ vanishes.

Benzi *et al.* (1993) find that the resulting $f_p(r)$ is the same for all p. In this case, the function f_p may be eliminated by plotting $G_p(r)$ against another moment $G_{p'}(r)$ (with e.g. $p' = 3$) in a log-log plot. This leads to considerable improvement of scaling behaviour. A comment on this so-called 'extended self-similarity' was given by van de Water & Herweijer (1995). Defining odd-order longitudinal moments in terms of absolute values of $\Delta u(r)$ ignores the skewness that we deem an essential property of the statistics of small-scale velocity fluctuations. Therefore we will always consider the proper moments $G_p(r) = \langle \Delta u^p \rangle$ throughout this paper. A trivial exception is the case of transverse velocity differences that are symmetric by definition and for which only even moments would be non-zero. The weak dependence on p of either the even- or the odd-order residual functions $f_p(r)$ will be studied in detail in § 7.1.

These various functional forms for structure functions should be viewed as first steps towards a finite-scale theory for turbulent scaling. Such a theory is expected to provide scaling functions that encompass a significantly larger scaling range, as it will include (part of) the viscous scales. In this respect the situation is similar to that of critical phenomena. Only after finite-scale corrections were formulated, could precise values for the critical exponents be extracted from experiments.

2.2. *Consequences of the multifractal model*

The multifractal model has a number of interesting consequences that are amenable to experimental verification. Deviations from inertial-range scaling, $G_p(r) \sim r^{\zeta(p)}$, due to the influence of viscosity occur at distances $r \approx 30\eta$. As the Reynolds number is not yet unity at these scales, the interval $[\eta, 30\eta]$ is called the intermediate viscous range. It turns out that the multifractal model leads to a prediction of $G_p(r)$ in this range that is related to a quite common property of fractals (Frisch & Vergassola 1991; Jensen, Paladin & Vulpiani 1991; and Wu *et al.* 1990). Scaling behaviour of natural fractal objects does not extend to arbitrary small length scales. In general, there exists a crossover length scale where fractal scaling stops and where a more trivial scaling regime is entered that displays, for example, the continuity of the object at the smallest scales. A multifractal exists of a whole collection of singularity strengths h and the crossover can depend on h. This presence of many crossover lengths will here be called *multiscaling*. A similar situation exists in turbulence. (Multi)fractal scaling ceases at scales where the influence of viscosity starts to be felt. This crossover point should depend on h as stronger singularities can survive to smaller scales before they are smoothed by viscosity. Because structure functions of increasing order p probe the singularities of increasing strength, the scaling behaviour of $G_p(r)$ should extend to smaller r as p increases.

The exact manner in which singularities are smoothed and the exact way in which the scaling extends more and more to viscous scales as p increases is a still unresolved question, but a crude model follows from equating the eddy turnover time $r/v(r)$ to the viscous momentum diffusion time r^2/ν, where ν is the kinematic viscosity and $v(r)$

is the velocity difference at scale r (Paladin & Vulpiani 1987). It then follows that for a given singularity strength h there is a smallest distance r_c to which scaling behaviour can extend. Conversely, for a given distance r, there is an upper limit to h, $h_{\max}$, corresponding to the weakest singularity that can survive at r. We will briefly discuss the derivation of $h_{\max}$, which closely follows that of Frisch & Vergassola (1991). We will then use it to compute a model $G_p(r)$ and illustrate the influence of multiscaling.

The dimensionless relation between velocity differences $v(r)$ at different scales r is

$$v(r) = v(L)\left(\frac{r}{L}\right)^h, \tag{2.6}$$

where L is an external length scale, for example the integral scale. The argument sketched here leads to

$$\left(\frac{r_c}{L}\right)^{h+1} = \frac{\nu}{Lv(L)} = Re^{-1}, \tag{2.7}$$

where ν is the kinematic viscosity. Using the relation $r_\nu/L = Re^{-3/4}$ between the external scale L and the viscous scale r_ν, it follows that

$$\frac{r_c}{r_\nu} = Re^{(3h-1)/(4h+4)}. \tag{2.8}$$

Experimental evidence, as for example shown in figure 17, points to the strongest singularity having a strength $h_{\min} \approx 0.16$ in which case (2.8) predicts a very weak dependence of the cutoff scale on the Reynolds number, $r_c/r_\nu \approx Re^{-0.1}$. The conclusion is that it will be difficult to see the dependence on Re in experiments that cannot span a large dynamical range of Reynolds numbers.

The influence of multiscaling on the structure function follows from

$$G_p(r) = \int_{h_{\min}}^{h_{\max}(r)} \mathrm{d}h \left(\frac{r}{L}\right)^{ph+3-D(h)}, \tag{2.9}$$

where $h_{\max}(r)$ is given by

$$h_{\max}(r) = \frac{4}{3}\frac{\log(r_\nu/L)}{\log(r/L)} - 1. \tag{2.10}$$

Although the dependence on the Reynolds number would be difficult to observe in laboratory-scale experiments, it should be possible to see the influence of multiscaling on the form of the structure function at a fixed Reynolds number. This is illustrated in figure 1 where $G_p(r)$ as computed from (2.9) is shown for $p = 2, 4$, and 8.† The (convex) function $D(h)$ was taken from an experiment (by Legendre transforming a measured structure function exponent $\zeta(p)$, with a few points at $D'(h) < 0$ taken from Meneveau & Sreenivasan 1991), but the outcome of the computation does not depend on the details of the assumed $D(h)$.

For this calculation we have assumed $L = 10^3$ and $r_\nu = 30$. We believe that these are reasonable numbers for laboratory turbulence and it is seen in figure 1 that the crossover distance shifts to smaller r as p increases. At the smallest r one expects the turbulence field to be smooth and $G_p(r) \sim r^p$. This behaviour is of course lacking in (2.9).

A second experimentally observable consequence of the multifractal model follows from the intrinsically geometric view of turbulent fluctuations. The model assumes that these fluctuations arise from interwoven sets of singularities. The probability of

† An asymptotic analysis for $Re \to \infty$ and $l \to 0$, leading to an analytic form for $G_p(r)$ has been given by Frisch & Vergassola (1991).

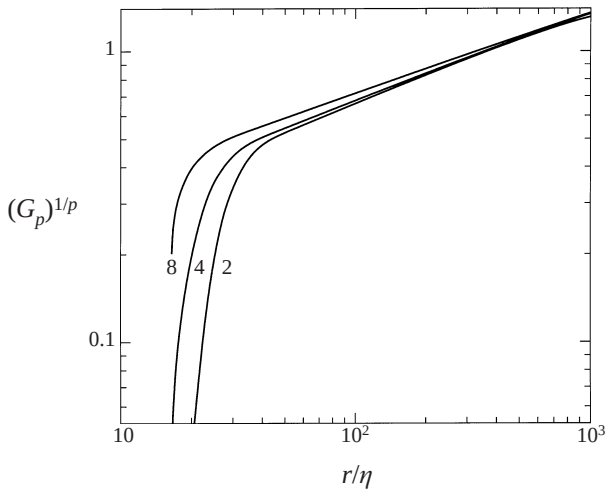

FIGURE 1. Multiscaling behaviour of structure functions: the scaling of structure functions extends deeper into the intermediate viscous range as the order becomes larger. The structure function $G_p(r)$ has been computed from (2.9), (2.10) and assuming a polynomial function $D(h)$ that is a fit to measured data. The inertial-range slope of the plot of $\log G_p(r)^{1/p}$ versus $\log r$ depends on p; the scaling anomaly is comparable to that found experimentally.

encountering a particular singularity at scale r is determined by the dimension $D(h)$ of the set in which this singularity exists. In the case of our longitudinal structure functions, velocity fluctuations are measured on a line that cuts through the turbulent flow field. It is a simple observation that the intersections of lines in three dimensions form an empty set.

A more precise statement about the geometry of intersections follows from the rule that in three dimensions the dimension $D_s(h)$ of the set of intersections of a line with the set of singularities h is given by $D_s(h) = -2 + D(h)$ (Mandelbrot 1990). In the case that $D_s(h) < 0$, the chances of encountering a singularity of strength h decrease with decreasing r, with the negative value of the dimension D_s signifying the manner in which the simultaneous intersection of a ball with radius r with both the line and the set of singularities becomes empty with $r \to 0$. Because at $D'(h) < 0$ the smallest value of $D(h)$ corresponds to the smallest h, the value of $h_{\min}$ given by $D_s(h_{\min}) = 0$ is limiting. In the case of longitudinal measurements $h^L_{\min}$ is determined by $D(h^L_{\min}) = 2$. Conversely, a measurement of transverse velocity differences in a planar cut of the turbulent field leads to the limiting value $h^T_{\min}$ with $D(h^T_{\min}) = 1$. Thus one expects to see stronger singularities in a transverse experiment. These results may be understood intuitively by imagining stringed singularities as the carriers of the strongest events in turbulence. The chances of detecting the associated exponents are bigger in an experiment that cuts a plane than in one that cuts a line.

According to the simple intersection argument, the behaviour of $\zeta(p)$ for large p of the multifractal model would be essentially different from that predicted by the log-normal model. In the latter model $\zeta(p)$ has a maximum, after which the scaling exponent bends down. In marked contrast, if a strongest detectable singularity exists, the scaling exponent for large p is

$$\zeta^L(p) = 1 + ph^L_{\min} \quad \text{and} \quad \zeta^T(p) = 2 + ph^T_{\min}, \tag{2.11}$$

for our longitudinal and transverse measurements, respectively.

The question about negative dimensions in turbulence is an interesting one and has been discussed by Chhabra & Sreenivasan (1991, 1992) and Molenaar, Herweijer & van de Water (1995).

3. Flow configuration and instrumentation

A central point of our experiments has been the design of laboratory flow configurations in which structure functions exhibit clear scaling behaviour that allows unambiguous determination of a scaling exponent. As Reynolds numbers in the laboratory are limited, our quest for ideal flows sometimes involved a compromise on isotropy of turbulent velocity fluctuations.

For experiments on longitudinal structure functions we have used a single probe whose time-dependent signal $u(t)$ was interpreted as a space-dependent signal $u(x)$ with $x = Ut$. The interpretation of time variation as space variation is the subject of Taylor's frozen turbulence hypothesis that has been discussed by Antonia, Phan-Tien & Chambers (1980). A key parameter that determines the applicabillity of Taylor's hypothesis is the relative size of the velocity fluctuations $u_{\rm rms}/U$, with $u_{\rm rms} = \langle u^2 \rangle^{1/2}$. For the transverse structure function we have used an array of probes which was oriented perpendicularly to the mean flow direction and no recourse to Taylor's hypothesis need be made. Spatial distances are now physical distances between pairs of probes. In our experiment the smallest distance is 3 mm, but microprobes that are separated by 0.5 mm (which is slightly larger than η) are under construction. For longitudinal measurements distances can be manipulated much more easily because they are equivalent to time delays which can be readily tuned electronically.

In both cases, usage of a single hot wire can only approximately discriminate between the two velocity components u, v perpendicular to the wire. The relative contribution of the v-component to the signal is again proportional to $u_{\rm rms}/U$. There is, as yet, no good analysis available for the influence of both the Taylor hypothesis and the v-contamination of the measured signal on high-order structure functions. In the present study we have used flows where the ratio $u_{\rm rms}/U$ varies approximately by a factor of 5, and the influence on high-order structure functions can be assessed only indirectly.

Another very important aspect of our experiments has been the design of novel instrumentation. This is detailed in § 3.2. In particular, we have strived for real-time processing of turbulence data. A real-time approach obviates the necessity of storage of the extremely voluminous primary data. These data consist of extremely long (many hours) time series of velocity fluctuations sampled at approximately the Kolmogorov frequency and measured at a single point or at several points simultaneously.

3.1. *Flow configuration*

The experiments were done in two distinct flows: grid-generated turbulent flow in a closed wind tunnel and a turbulent flow that emanated from a jet. The flow conditions are summarized in table 1. Several slightly different arrangements were used for the grid flow, leading to slightly different characteristics; those have also been detailed in table 1.

The wind tunnel has an experiment section of 8 m length with a $0.7 \times 0.9 \mathrm{m}^2$ cross-section. Turbulence was generated by a grid at the beginning of the experiment section. The grid consisted of a planar mesh of 0.1 m and 34% solidity. The isotropy of the turbulent velocity fluctuations for a similar grid has been extensively studied by Comte-Bellot & Corrsin (1966).

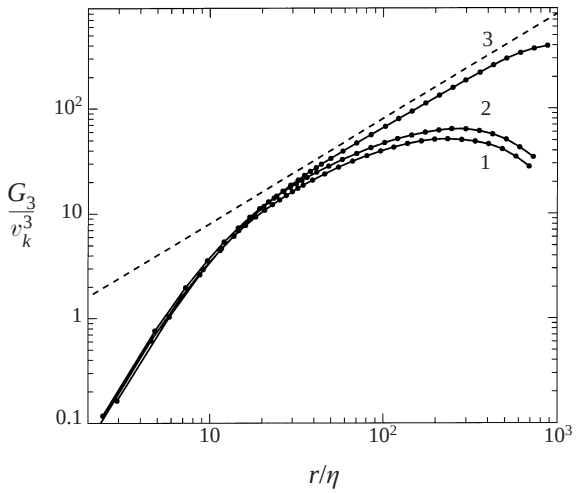

FIGURE 2. Normalized third-order longitudinal structure functions measured in grid turbulence (2 of table 1). Curve 1 is measured with the probe on the centreline of the grid; here the Reynolds number is smallest, $R_\lambda = 1.9 \times 10^2$. For curves 2 and 3, the distance to the wind-tunnel boundary is 0.17 m and 0.07 m, with Reynolds numbers $R_\lambda = 2.6 \times 10^2$ and $R_\lambda = 5.3 \times 10^2$, respectively. The dashed line is $|G_3/v_k^3| = 4r/5\eta$.

Configuration	U (m s^{-1})	$u_{\rm rms}$ (m s^{-1})	Re_λ	η (m)	L (m)	l_p/η	$U/f_s\eta$
1	12.6	0.68	3.4×10^2	2.0×10^{-4}	0.095	1	3
2	11.0	0.94	5.3×10^2	1.9×10^{-4}	0.17	1	3
3	12.2	1.05	6.0×10^2	1.8×10^{-4}	0.13	1	3
4	10.4	0.80	4.5×10^2	2.0×10^{-4}	0.17	1	2
5	11.4	0.95	5.6×10^2	1.9×10^{-4}	0.15	1	3
6	12.5	2.27	8.1×10^2	9.5×10^{-5}	0.075	2	6

TABLE 1. Characteristic parameters of the turbulent flows used. The mean velocity is U with $u_{\rm rms} = \langle u^2 \rangle^{1/2}$ the r.m.s. size of the fluctuations. For the definition of the other characteristic quantities the r.m.s. derivative velocity $\dot{u}_{\rm rms} \equiv \langle (\mathrm{d}u/\mathrm{d}t)^2 \rangle^{1/2}$ is used. For the mean energy dissipation ϵ the isotropic value is taken $\epsilon = 15\, \nu \dot{u}_{\rm rms}^2\, U^{-2}$ with ν the kinematic viscosity. The Kolmogorov scale is $\eta = (\nu^3/\epsilon)^{1/4}$ and the Taylor microscale is $\lambda = U u_{\rm rms}/\dot{u}_{\rm rms}$ with the associated Reynolds number $Re_\lambda = \lambda u_{\rm rms}/\nu$. The integral length scale is defined in terms of the correlation function of velocity fluctuations $L = \int_0^\infty \langle u(x)u(x+r)\rangle_x \mathrm{d}r/\langle u^2 \rangle$. The following flow conditions have been used: (1) Turbulence 3 m behind a grid with mesh size 0.1 m and 0.34% solidity in a wind-tunnel with cross-section 0.9 m vertical and 0.7 m horizontal. The probe was located in a region of non-zero mean flow gradient, $h = 0.19$ m from the wind-tunnel boundary. (2) Same as (1) but the vertical size of the wind-tunnel test section was reduced to 0.5 m and $h = 0.07$ m. (3) Same as (1) but the mean flow gradient was increased by increasing the solidity of the grid mesh closest to the walls to 0.7%. (4) Same as (1) but $h = 0.07$ m. (5) Same as (1) but $h = 0.1$ m. (6) Jet turbulence. The jet flow emanated at 30 m s^{-1} from a 12 cm diameter jet. Data were taken 2.6 m downstream on the jet centreline. In order to quantify the degree of averaging over small structures, we also quote the ratio l_p/η of the probe length l_p and the Kolmogorov length η and the ratio $U/f_s\eta$ of the Kolmogorov frequency, U/η and the sampling frequency f_s.

In grid turbulence, isotropy is most closely approached at the centreline of the grid. However, as here the decay of turbulence is strongest, this is not the optimal location to study scaling phenomena. Figure 2 shows the third-order structure function $G_3(r/\eta)/v_k^3$ as a function of position. It appears that a scaling range is absent at the grid

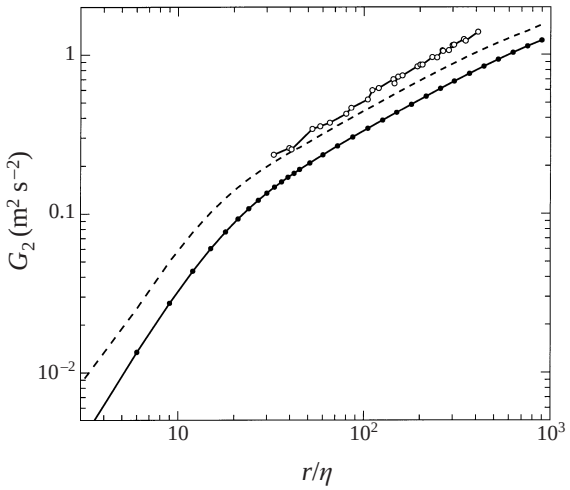

FIGURE 3. Comparison of second-order longitudinal and transverse structure function measured in grid turbulence (5 of table 1). Open circles: transverse $G_2^T(r)$; dots: longitudinal $G_2^L(r)$. Dashed line: transverse structure function $\widetilde{G}_2^T(r)$ computed from the measured longitudinal $G_2^L(r)$ using (2.2). The difference between $\widetilde{G}_2^T(r)$ and $G_2^T(r)$ is a measure of the degree of anisotropy of the flow.

centreline, where the Taylor microscale Reynolds number is smallest ($Re_\lambda = 1.9 \times 10^2$). The best scaling behaviour, the largest value of Re_λ, and the best agreement with the inertial range prediction $G_3(r/\eta)/v_k^3 = -\frac{4}{5}r/\eta$ is obtained at about 0.07 m from the wall. Clearly, this close proximity to the wall entails the biggest compromise to isotropy of the largest scales, although the measured prefactor C_3 in the scaling law $G_3(r) = -C_3\epsilon r$, $C_3 = 0.72$, is quite close to the theoretical one, $C_3 = 4/5$. The influence of the large-scale flow structure on small-scale statistics has been discussed by Kuznetsov, Praskovsky & Sabelnikov (1992), who show the variation of C_3 and μ with the degree of large-scale intermittency.

One test of isotropy is the measurement of C_3; by also considering the viscous term in (2.1), such a test can be extended to scales where viscosity is important (Antonia, Chambers & Browne 1983). A much more direct check of isotropy, however, is the comparison of transverse and longitudinal second-order structure functions through the isotropy relation (2.2). This comparison is done in figure 3 in grid turbulence where the sensor array is parallel with the wall at a distance $h = 0.1$ m. With the length of the array 0.078 m and the width of the wind-tunnel test section 0.7 m, we assume the flow to be homogeneous over the sensor array. Obviously, in figure 3 (2.2) is best satisfied at the smallest distances $r/\eta \approx 30$ where the velocity fluctuations are closest to isotropic whereas marked discrepancies can be seen at the largest separations.

Other flow conditions show a closer approach to isotropy at larger scales r/η, but the Reynolds number is smaller here and a scaling region where $G_3^L(r) \simeq r$ is virtually absent. We believe that the compromise found between isotropy and a large enough Reynolds number so that scaling can be seen is typical for laboratory flows. We are not aware of other isotropy studies in relation to the measurement of high-order structure functions. Still, this is an important issue because large-scale anisotropy may affect scaling exponents. Transverse experiments have been restricted to wind-tunnel flow because of the better temperature stability in the wind-tunnel. As will be explained in § 3.2, this stability is of crucial importance for the calibration reproducibility of a multi-probe array.

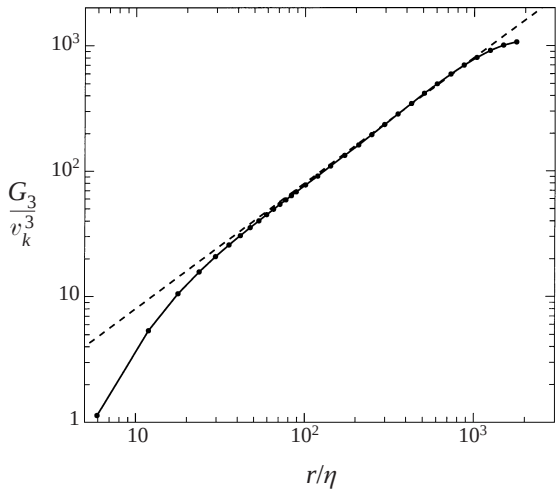

FIGURE 4. Normalized third-order longitudinal structure function measured in jet turbulence (6 of table 1). Dashed line: $|G_3/v_k^3| = 4r/5\eta$.

Longitudinal structure functions have also been measured in jet turbulence. Here, turbulence was generated by the efflux of a jet through a $D = 12\,\mathrm{cm}$ diameter nozzle in still air. The flow exited in open laboratory space and obstacles were at least 5.5 m downstream. Longitudinal turbulent velocity fluctuations were measured at a distance $x/D = 22$ through processing of the time-dependent velocity signal. For these experiments the Reynolds number is $Re_\lambda \approx 10^3$ and structure functions show a clear and unambiguous scaling behaviour. This is demonstrated for the third-order structure function in figure 4. However, because the velocity fluctuations are large ($u_{\mathrm{rms}}/U \approx 0.25$), application of Taylor's hypothesis is more questionable here than in our longitudinal grid-turbulence experiments where u_{rms}/U ranges from 0.05 to 0.09. In figure 4 the experimental C_3 is close to the theoretical $C_3 = 4/5$; however, in other experiments larger deviations were seen.

Another setup that is commonly used for the study of turbulent scaling behaviour is cylinder turbulence. For these experiments we have used an 11 cm diameter cylinder that was placed in our windtunnel. Velocity fluctuations were measured at a downstream location $x/D = 54$, where x is the distance to the cylinder axis. In these experiments, that were done with mean flow velocities up to $20\,\mathrm{m\,s^{-1}}$, we have not been able to observe convincing scaling behaviour of G_3.

3.2. *Instrumentation*

Constant-temperature hot-wire anemometry was used to measure the turbulent velocity fluctuations. The velocity probes were made of $d_p = 2.5\,\mu\mathrm{m}$ diameter platina–wolphram wire with a sensitive length of $l_p = 200\,\mu\mathrm{m}$. The wire was stretched between 10 mm long, 0.5 mm base-diameter Nimonic 90 prongs that were separated by 3 mm. In order to avoid flow-induced mechanical resonances of the probes, special care was given to the construction and choice of materials. The prongs were mounted in thin (3 mm diameter) ceramic tubes.

The effective length l_p of the probes is in all our experiments of the order of the Kolmogorov length η. It should be noted, however, that our wires are relatively thick. This results in relatively large end-conduction losses of the hot wire. It has been surmised that in this case the frequency response is not flat due to the frequency dependence

of end- conduction losses. This idea was tested by Bremhorst & Gilmore (1976) for probes with $l_p/d_p > 200$. However, measured dynamical (frequency-dependent) calibration curves did not significantly differ from a static calibration. We have performed similar, but more precise dynamic calibrations and also failed to see an effect on our probes (that have $l_p/d_p \approx 80$).† Still, it is very well possible that even smaller values of l_p/d_p would be detrimental for the frequency response of the probe.

We have noticed slight quantitive changes in the course of our experiments which we attribute to probe artifacts that are not completely understood. For example, in repetitions of the same jet experiment but with different probes we have found significant variations in $\zeta(3)$ that ranged from 0.95 to 1.03. The probes that have been used have been especially designed for this type of study. They necessarily are a compromise among mechanical rigidity, calibration stability and accuracy, and further progress needs be made to perfect them.

For the transverse measurements, initially a rake was used with five probes placed such that their ten distances were optimally spaced on a logarithmic scale. By adding three more probes symmetrically, nine distances come in pairs. Although eight probes give 28 distances that could be distributed more evenly over the (log) r-axis, we have chosen to cluster points in pairs. This allowed a check on statistical accuracy and systematic errors.

A precise and stable calibration of the probes is crucial for transverse measurements where, at a particular separation, we measure velocity differences with two different probes. The probe output voltage is a strongly nonlinear function of the wind velocity. A slight change of the probe characteristics, caused for example by a drift of the ambient temperature, results in a drift of the working point on the calibration curve. The result is an apparent change of the mean velocity and an apparent change of the probe sensitivity. It is easy to correct for the first effect when analysing results, but accounting for the second effect is impossible in a real-time setup. For longitudinal measurements with a single probe, a change of the probe sensitivity results in a slight apparent shift of the inertial range, However, for transverse measurements such a change results in a catastrophic asymmetry of measured probability density functions. A measure for the quality of transverse experiments, therefore, is the symmetry of the measured PDF under reflection of the velocity difference axis. Therefore, we will always show $P^T(\Delta u)$ and $P^T(-\Delta u)$ superposed on a single graph. This symmetry test is necessary but not sufficient and further confidence in the results must be gained from repeated experiments.

In order to cure the calibration problem, we have adopted a strict procedure in which calibration curves are registered immediately prior to experimental runs. For the transverse measurements this procedure is completely automated with help of a computer that places a calibration nozzle in front of each of the probes and automatically registers a calibration curve. Calibration data were fitted with fourth-order polynomials which were used to generate 12×12 bit calibration tables.

The probes were instrumented with locally manufactured computer controlled anemometers and adjustable amplifiers. The signals were passed through 4-pole constant-phase anti-aliasing filters and digitized with 12 bits. The conversion of measured voltages to wind velocities was done using 12×12 bit lookup tables. The

† Bremhorst & Gilmore (1976) measured dynamic calibration curves by shaking the probe. In our experiments the overheat ratio was periodically varied. By phase-synchronous averaging, very accurate dynamic calibration curves can be measured. No difference with static calibration curves was found.

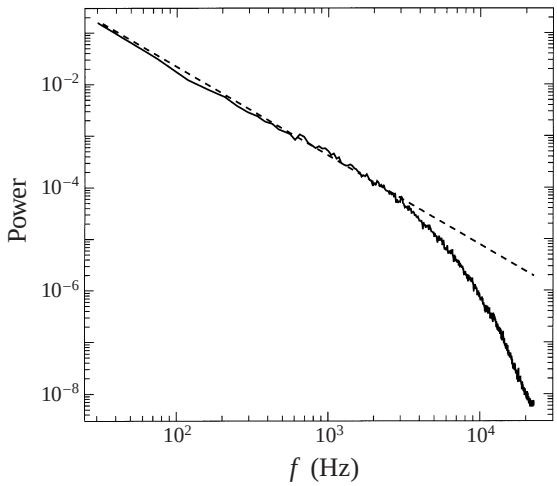

FIGURE 5. Power spectrum of turbulent velocity fluctuations measured in jet turbulence (6 of table 1). The vertical axis spans the entire dynamical range of a 12-bit ADC. The dashed line is a fit to the spectrum; it has slope -1.72.

Kolmogorov length η is the smallest length scale in the flow, and correspondingly $f_k = U/\eta$ is the largest frequency in the turbulent signal. For measuring structure functions, the anti-aliasing filter cutoff frequency f_c and the sampling frequency f_s should ideally be set at f_k and $2f_k$, respectively. As f_k increases, for example with increasing Re_λ, both the physical size and the magnitude of the velocity difference of the smallest eddies in the turbulent flow decrease. The smallest detectable size is determined by the size of the probe l_p and by f_c. The smallest detectable velocity fluctuation is determined by the dynamical range of the ADC that must accommodate both the largest and the smallest velocity fluctuations of the flow. In our jet experiments we have reached the maximum dynamical range of the 12 bits ADC. Figure 5 shows a power spectrum of velocity fluctuations in a jet with $Re_\lambda \approx 8 \times 10^2$ and $f_k \approx 50$ kHz. The sampling frequency is $f_s = 45$ kHz, the filter cutoff $f_c = f_s/2$, and the span of the vertical axis is approximately 2^{24}. For this experiment, an increase of the sampling frequency appears useless without an increase of the number of bits in the digitization of the velocity signal. This would, incidentally, only be worthwhile with a simultaneous redesign of the anemometry circuitry. A higher precision is important for smaller velocity differences. As our main interest is the statistics of large velocity differences, an increase of the discretization accuracy does not seem urgent. We finally note that the spectrum of figure 5 is without spurious peaks. It reflects a concentrated effort to carefully shield noise sources and suppress mechanical resonances.

Statistically accurate measurements of high-order structure functions need long integration times. In a conventional approach to turbulence data processing, long integration times imply the registration and storage of long times series of measured velocities. This inevitably leads to storage problems and long processing times before the result of the experiment (PDFs, structure functions) becomes available.

In all of our experiments, we employ real-time processing of velocity differences. For the longitudinal experiments we have built a special digital device that can measure high-order structure functions in real time through accumulated probability density functions of $\Delta u(r)$. Not only has this significantly eased the statistics problem, but the absence of stored time series and the immediate availability of the structure function

has allowed systematic experimentation with the flow conditions (Herweijer *et al.* 1994). The maximum number of velocity samples that we have taken is 1.5×10^9, which is two orders of magnitude larger than in Anselmet *et al.* (1984).

The 'structurator' accepts 12-bit anemometer voltages that are converted to wind velocities using a lookup table and fed into a long (1024 positions) circular buffer. Velocity diferences $u(t) - u(t + \tau_i)$ are computed at discrete values of τ_i which are spaced exponentially on $[\tau_s, 1024\tau_s]$, where τ_s is the sample time. The version of the structurator used operates in real time at a sampling rate of 20 kHz ($\tau_s = 5 \times 10^{-5}$s).†

For the transverse experiments we have used a real-time instrumentation computer and coded crucial parts of the acquisition program in machine language. An effective throughput of about 5 kHz (for eight hot wires) was achieved, which is a factor of four smaller than the optimal acquisition speed that is determined by f_k.

4. Probability density functions

In an experiment on the small-scale structure of turbulence one would collect probability density functions (PDFs) of velocity differences and compute their moments afterwards. Scaling arguments apply directly to the structure functions but it is of interest to study the intermediate PDFs. First we will compare measured longitudinal and transverse probability density functions. We will then analyse these experimental PDFs in terms of an intermittency model. Finally we will discuss a simple but adequate functional form for the tails of the PDF which can be used for a better control of the statistical convergence of high-order moments.

4.1. *Longitudinal and transverse probability density functions*

Figure 6 compares transverse $P^T(\Delta u)$ and longitudinal $P^L(\Delta u)$ probability density functions at several separations r. It is a striking observation that for separations that are approximately in the inertial range ($r/\eta \lesssim 200$) the negative velocity difference tail of the (skewed) P^L coincides with the tails of the transverse P^T. As has been emphasized in § 3.2 the transverse PDFs $P^T(\Delta u)$ have been measured using two separate velocity probes and the accuracy of the probe calibration is crucial. Calibration and inhomogeneity problems may show in an asymmetry of the PDF and we always superimpose $P^T(\Delta u)$ and $P^T(-\Delta u)$. In a few cases the asymmetry just exceeds the noise level of the PDFs.

Inspection of the probability density functions shows that the probability of finding a large negative velocity difference $-|\Delta u|$ in a longitudinal measurement is 3 to 4 times larger than finding the companion positive $|\Delta u|$; consequently the value of the longitudinal velocity moments is mainly determined by the negative tails of the probability density function $P^L(\Delta u)$. This is nicely demonstrated in figure 7 which shows $F_r^L(p) = |\langle \Delta u^p(r) \rangle|^{1/p}$ as a function of p for two values of r that correspond to the bounds of the inertial range. For $p \gtrsim 8$, $F_r^L(p)$ at even values of p can to a good approximation be interpolated between $F_r^L(p-1)$ and $F_r^L(p+1)$ at neighbouring odd values, and vice versa. The scaling of G_p^L, therefore, is for large p mainly determined by $\Delta u < 0$. The comparison between longitudinal and transverse PDFs in figure 6 is put into another perspective in figure 7 through contrasting longitudinal and transverse F_r. As is already suggested in figure 6, the difference between longitudinal

† A software version running at 100 kHz has now been implemented using a standard Digital Signal Processing chip.

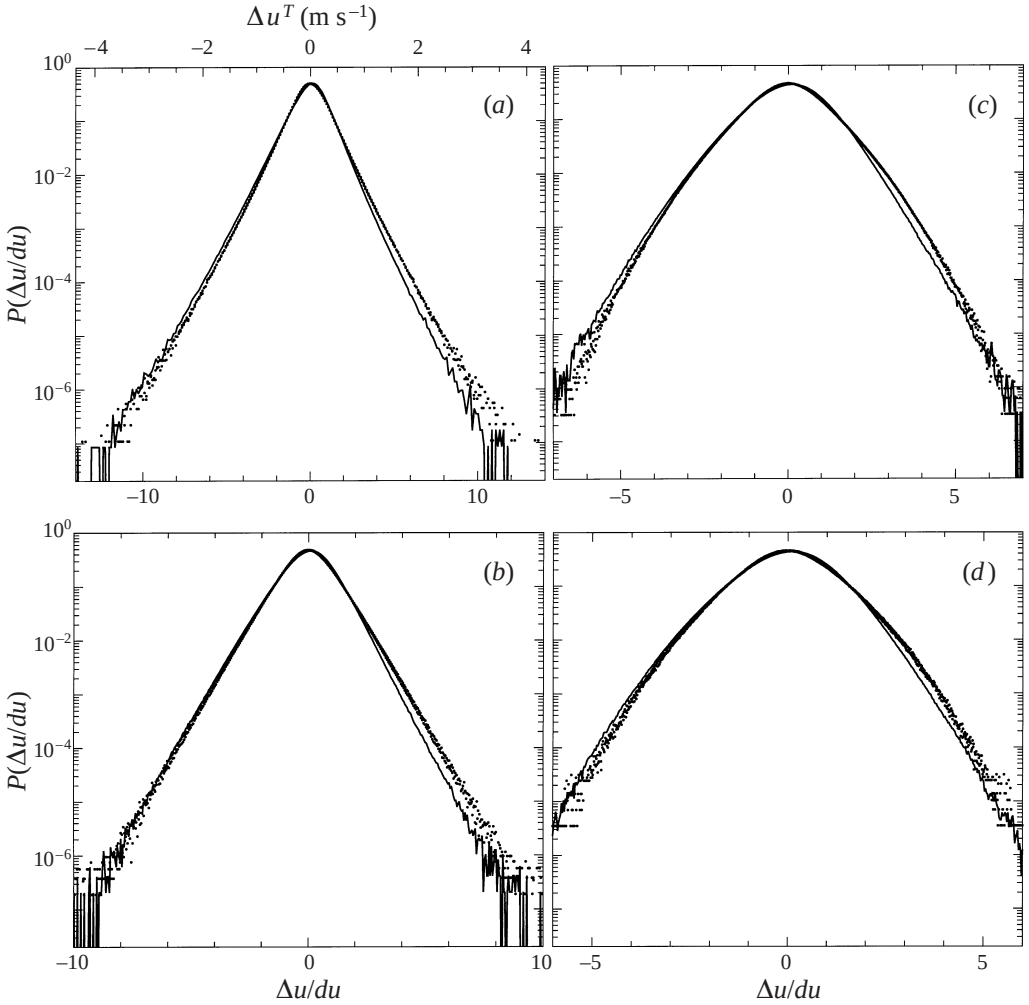

FIGURE 6. Transverse and longitudinal probability density functions of velocity differences measured in grid turbulence (5 of table 1). Dots: superposition of transverse $P_r^T(\Delta u)$ and $P_r^T(-\Delta u)$, lines: longitudinal $P_r^L(\Delta u)$ probability density functions. The separations are (*a*) $r/\eta = 9$ for P_r^L and P_r^T; (*b*) 36 for P_r^L and P_r^T; (*c*) 150 for P_r^L and 135 for P_r^T; (*d*) 260 for P_r^L and 250 for P_r^T. The probability density functions have been normalized such that $\int P(y)\mathrm{d}y = 1$, $\int yP(y)\mathrm{d}y = 0$ and $\int y^2P(y)\mathrm{d}y = 1$. The r.m.s. velocity difference du is defined as $du \equiv \langle (u(x+r) - u(x))^2 \rangle_x^{1/2}$. An absolute scale for the transverse velocity difference has been given for plot (*a*).

and transverse moments grows with decreasing separation. We will show in § 7 that this is consistent with a stronger anomaly of $\zeta^T(p)$.

In all the PDFs shown, we have normalized the velocity scale at a particular separation r by the corresponding root-mean-square velocity difference $du \equiv \langle [u(x+r) - u(x)]^2 \rangle^{1/2}$. The velocity scales $du^{T,L} = (G_2^{T,L})^{1/2}$ of P^T and P^L, respectively, are related through the isotropy relation (2.2). This relation predicts that for nominal inertial-range scaling, $G_2(r) \simeq r^{2/3}$, the transverse du^T is a factor $(4/3)^{1/2}$ larger than the longitudinal du^L, but the ratio grows to $2^{1/2}$ as r reaches the viscous scales. On an absolute velocity scale, therefore, transverse velocity differences can become very large. In figure 6(*a*) we have provided an absolute velocity scale

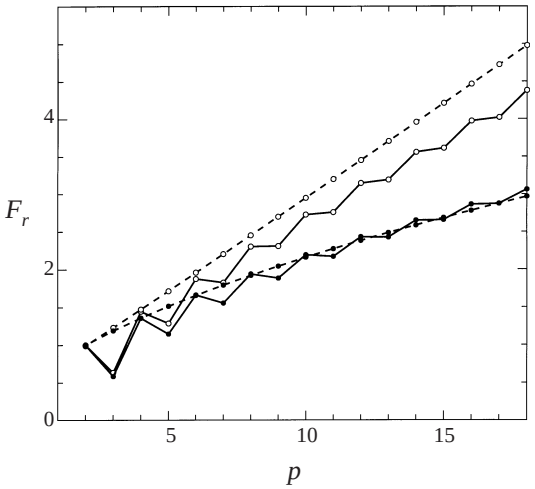

FIGURE 7. Structure function of grid turbulence (4 in table 1). Shown is $F_r^{L,T}(p) = |\langle \Delta u(r)^p \rangle|^{1/p}$ as a function of the order p at two separations inside the inertial range: $r/\eta = 33$ (open circles) and $r/\eta = 440$ and 410 (closed dots) for the longitudinal and transverse case, respectively. Dashed lines are F_r^T, full lines F_r^L. The normalization is $F_r^{L,T}(2) = 1$. The divergence with increasing p of the curves corresponding to the two separations is an expression of anomalous scaling of $G_p(r)$.

for the transverse $P_r^T(\Delta u)$ at $r/\eta \approx 9$. For this experiment the mean velocity was $U = 13\,\mathrm{m\,s^{-1}}$, with the r.m.s. velocity fluctuation a mere 3.5% ($u_{\mathrm{rms}} = 0.46\,\mathrm{m\,s^{-1}}$). Still, during an experimental run that effectively lasted approximately 100 minutes, we have detected velocity differences as large as $4\,\mathrm{m\,s^{-1}}$ across $r = 3\,\mathrm{mm}$.

Although the size of the transverse velocity differences is surprising, it could have been anticipated on the basis of the longitudinal probability density functions. We have demonstrated that the $\Delta u < 0$ tail of the normalized longitudinal and transverse PDFs approximately coincide, so that the transverse excusions are only a factor $2^{1/2}$ (that is the ratio $\mathrm{d}u^T/\mathrm{d}u^L$) larger than the longitudinal ones. We emphasize that it is not the absolute scale of the velocity differences that is of prime interest in scaling arguments, but the way these velocity differences increase with increasing separation. This dependence determines the exponents $\zeta(p)$ and reflects the strengths of the singularities involved. Not only is the absolute scale of transverse velocity differences larger, but, as we will show in § 7.3, transverse velocity differences also correspond to significantly stronger singularities.

4.2. *Models for probability probability density functions*

Intermittency models, such as those summarized in § 2, give also rise to models for the probability density function of velocity differences. Roughly, these models express that the probability distribution of velocity differences at scale r is inherited from that at large scales through a self-similar refinement process. The large-scale PDF P_L is nominally Gaussian. At scale $r < L$, the resulting PDF P_r is a superposition of Gaussians that have a range of widths. Each of those Gaussians is thought to be spawned from P_L through a cascade process and, accordingly, the range of widths increases as r decreases. The distribution over those widths can itself be a Gaussian with width say λ (Castaing *et al.* 1990; Chabaud *et al.* 1994)

$$P_r(x) = \int \frac{1}{\lambda}\frac{1}{(2\pi)^{1/2}} \exp\left(-\frac{\ln^2\sigma}{2\lambda^2}\right)\frac{1}{\sigma} P_L\left(\frac{x}{\sigma}\right) \mathrm{d}\ln\sigma. \tag{4.1}$$

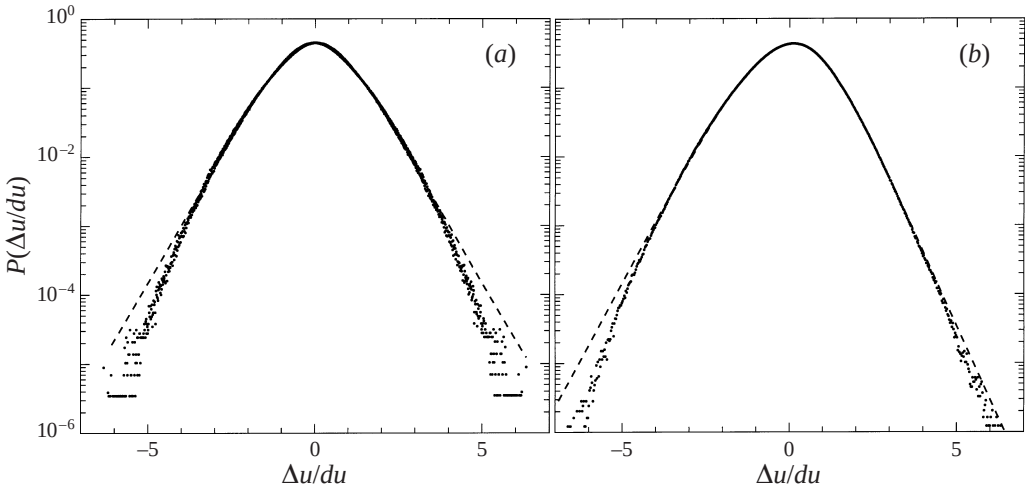

FIGURE 8. Comparison of probability density functions measured in grid turbulence (5 in table 1) with a multifractal model. (*a*) Dots: transverse probability density $P_r^T(\Delta u)$ and $P_r^T(-\Delta u)$ at $r/\eta = 250$. Dashed line: fit of (4.1) with $\lambda = 0.258$. (*b*) Dots: longitudinal probability density $P_r^L(\Delta u)$ at $r/\eta = 260$. Dashed line: fit of (4.1) with $\lambda = 0.212$. Skewness was incorporated in P_L as in Chabaud *et al.* (1994).

The parameter λ is an adjustable parameter whose value should increase with decreasing separation r. In the multifractal model the width σ of P_L depends on the number of cascade steps L/r and the singularity strength h as $\sigma \sim (L/r)^h$. The probability density function of widths is then given by the probability $(r/L)^{3-D(h)}$ of encountering in three dimensions a singularity h that resides in a set with dimension $D(h)$.

Equation (4.1) can then be rewritten as

$$P_r(x) \sim \int \left(\frac{r}{L}\right)^{3-\mathrm{D}(h)} P_L(x\,[r/L]^{-h})\mathrm{d}h, \tag{4.2}$$

and it is seen that the Gaussian distribution over widths in (4.1) is the approximation of $r^{3-\mathrm{D}(h)}$ near its quadratic maximum. Therefore, $\lambda^2(r) = \ln(r/L)/D''(\tilde{h})$, where $D''(\tilde{h})$ is the second derivative at the point $\tilde{h}$ where $D(h)$ reaches a maximum. Surprisingly, Chabaud *et al.* (1994) found that $\lambda^2(r) \sim r^{-\beta}$, which is not compatible with scaling behaviour of the moments $G_p(r)$. A representation of the PDF as a sum of Gaussians was earlier proposed by Benzi *et al.* (1991) and Kailasnath, Sreenivasan & Stolovitsky (1992); the difference with (4.1) is that the PDF is here a discrete sum over (binary) cascade steps.

The dependence of λ on r is of interest, but the primary question is if this model can be used to adequately represent PDFs. Figure 8 shows the result of a fit of (4.1) to measured longitudinal and transverse PDFs at approximately the same value of r/η in the inertial range. The value of the width parameter λ was determined with a careful least-squares procedure (see § 6). From results that are not shown it appears that for small distances $r/\eta \lesssim 30$, both longitudinal and transverse PDFs can be represented well with help of (4.1). However, discrepancies grow as r increases. This is illustrated in figure 8 for $r/\eta = 250$. The discrepancy is significant for the tails of the transverse $P_r^T(\Delta u)$, and, consistently, for the negative Δu tail of the longitudinal $P_r^L(\Delta u)$. We also point out that the value of λ differs significantly for the two cases. The conclusion is that measuring intermittency parameters through fitting models

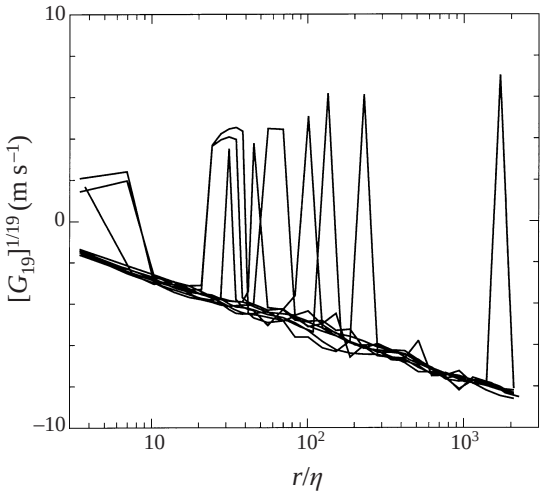

FIGURE 9. The variation of a large-order moment ($G_{19}(r)$) in repeated runs of a jet experiment (6 in table 1). Shown is the quantity $G_{19}^{1/19}(r) \equiv |\langle \Delta u^{19} \rangle|^{1/19} \times \text{sign}\langle \Delta u^{19} \rangle$ for 10 subsequent runs, each lasting $L/U \approx 10^5$ integral time scales (3×10^7 samples).

like (4.1) to PDFs cannot yet be a substitute for the measurement of scaling through high-order moments. It is especially at large p that discrepancies such as shown in figure 8 become important.

The tails of the probability density function evolve from exponential at small separations r to Gaussian at large separations where differences of essentially uncorrelated velocities are taken. This observation suggests a simple form for the tails of the PDF in terms of stretched exponentials (Kailasnath *et al.* 1992)

$$P(\Delta u) = a \exp(-\alpha |\Delta u|^{\beta}), \tag{4.3}$$

where the parameters a, α and β depend on the separation r and on the sign of Δu (they can be different for the left and right tail of $P^L(\Delta u)$). At small separations r, $\beta \approx 1$ and $P(\Delta u)$ is close to exponential; at large separations $\beta \approx 2$ and $P(\Delta u)$ becomes Gaussian. Contrary to the intermittency model of (4.2), the stretched-exponential description is not based on first principles and should be merely viewed as a convenient parametrization. In § 6 we will investigate the adequacy of this description and show how to determine its parameters. We will then use it to achieve a better control over the statistical convergence of high-order moments.

5. Statistical convergence of moments

The structure functions follow from the probability density functions as

$$G_p(r) = \int_{-\infty}^{\infty} P_r(x) x^p \mathrm{d}x, \tag{5.1}$$

where in practice the integration is replaced by a sum over non-empty bins of a discretized experimental $P_r(\Delta u)$ and the integration bounds are replaced by the largest and smallest Δu that occur in an experimental run.

Figure 9 illustrates the convergence problem by showing $\left(G_{19}^L(r)\right)^{1/19} \equiv |\langle (\Delta u)^{19} \rangle|^{1/19} \times \text{sign}\langle \Delta u^{19} \rangle$ for 10 subsequent runs of a jet experiment; each run is an average over 10^5

integral scales (3×10^7 samples). Because of the skewness of longitudinal PDFs, the moment shown should be negative, but it is seen that in some runs at some separations, notably in the inertial range, $G_{19}^L(r)$ almost perfectly reverses sign. Clearly, this large-order moment has not statistically converged at 3×10^7 samples and is determined by single events. Consequently, the integrand in $G_{19}^L(r) = \int P_r^L(x)x^{19}\mathrm{d}x$ has not returned to zero for the largest measured velocity differences.

A study of the convergence problem can be done in two ways. In § 5.1 we will use the correlation structure of moments in order to arrive at an estimate of the error in measured moments as a function of the integration time. In § 5.2 the largest moment G_p that is statistically meaningful for a given integration time will be estimated from the known statistics of measured PDFs.

5.1. *Using the correlation structure*

The accuracy of measured moments increases with the integration time T. The key point of an error estimate is that T must be expressed in terms of the correlation time of these moments. Assume that the true ensemble (or long-time) mean $\langle \Delta u^p \rangle$ is estimated by an average $\langle \Delta u^p \rangle_T$ over a finite integration time T. It is then possible to derive a simple expression for the root-mean-square error in $\langle \Delta u^p \rangle_T$ (Tennekes & Lumley 1972). This expression holds irrespective of the probability density function of Δu:

$$\langle \left[\langle \Delta u^p \rangle_T - \langle \Delta u^p \rangle \right]^2 \rangle^{1/2} \approx \left(\frac{I_p}{T} \right)^{1/2} 2 \langle \left[\Delta u^p(t') - \langle \Delta u^p \rangle \right]^2 \rangle_{t'}^{1/2}, \tag{5.2}$$

where $\Delta u^p(t)$ is the velocity difference over a distance r at time t and raised to the power p. It is clearly the ratio of T and the integral time I_p that is of relevance,

$$I_p = \int_0^\infty \rho_p(\tau)\mathrm{d}\tau, \tag{5.3}$$

with $\rho_p(\tau)$ the time-correlation function of Δu^p:

$$\rho_p(\tau) = \frac{\langle \left(\Delta u^p(t') - \langle \Delta u^p \rangle \right) \left(\Delta u^p(t' - \tau) - \langle \Delta u^p \rangle \right) \rangle_{t'}}{\langle \left(\Delta u^p(t') - \langle \Delta u^p \rangle \right)^2 \rangle_{t'}}. \tag{5.4}$$

For $p = 1$, the integral time $I_{p=1}$ gauges the integration time needed for the average velocity difference to converge to zero. In this case all necessary information can be obtained from the second-order structure function. In order to estimate the error in the moment of order p, knowledge about the moment of order $2p$ is needed. Because such an estimate needs the moment $G_{2p_{\max}}$, the method sketched here cannot be used to compute the largest meaningful moment $G_{p_{\max}}$ that can be measured for a given integration time. Nevertheless, it is useful and instructive to measure the expected error for a few low- order moments. The correlation functions of longitudinal velocity differences, (5.4), and associated integral times, (5.3), were computed from a stored time series (of length $10^5 L$) of velocity measurements in jet turbulence; time τ and the spatial separation δ are related through Taylor's hypothesis, $\delta = U\tau$.

The predicted error is shown in figure 10. Due to intermittency, the tails of the PDFs become wider with decreasing separation. Therefore, the error in high-order moments should increase as the separation r decreases and the effect of intermittency grows stronger. This trend is opposite to that for low-order odd moments that gauge the deviation from Gaussianity. At large separations, the PDF is close to Gaussian, and the error should increase with increasing separation. The crossover between these opposing trends is clearly seen in figure 10. The estimated error increases rapidly with

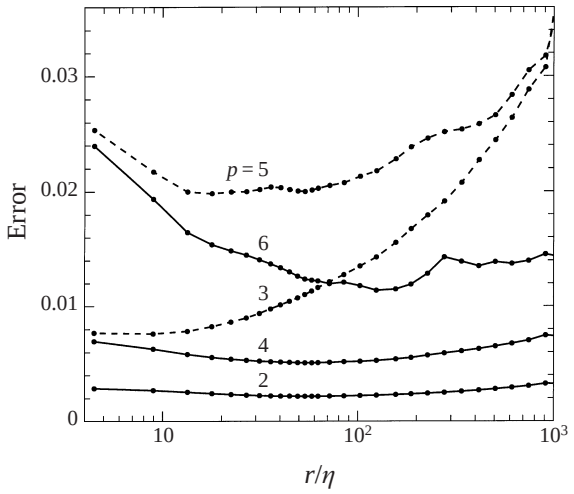

FIGURE 10. Error of structure function $\langle(\langle\Delta u^p\rangle_T - \langle\Delta u^p\rangle)^2\rangle^{1/2}$ (5.2) as a function of the order p. It was computed from a stored time series of velocities in jet turbulence (6 in table 1). The length of the time series is $T = 1.4 \times 10^5 L/U$.

increasing p and is largest for the odd moments. This result also illustrates that the statistical error of low-order moments at the integration times used is small and we conclude that the main source of uncertainty is systematic errors that are for example associated with the non-ideal realization of homogeneous and isotropic turbulence.

5.2. *Using the statistical error of the PDF*

A simple and practical estimate of the convergence time starts with the probability density functions of velocity differences. The PDF measures the number of times n that a given velocity difference Δu has occurred. A long experimental run contains a very large number of uncorrelated events and it is reasonable to assume that the probability distribution of n, $\mathscr{P}(n)$, is that of a Poisson process with $\mathscr{P}(n) = \langle n\rangle^n \exp(-\langle n\rangle)/n!$. The average number of times that a given velocity difference Δu has occurred in N velocity samples is $\langle n\rangle = NP(\Delta u)$ and the standard deviation of n is $\langle(n - \langle n\rangle)^2\rangle^{1/2} = \langle n\rangle^{1/2}$. For large n, $\mathscr{P}(n)$ becomes a Gaussian.

These statistical properties are demonstrated for measured probability density functions by subtracting the smooth part $\widehat{P}$ of a measured PDF such that its fluctuations remain. The smooth part was found by piecemeal fitting the log of $P(\Delta u)$ with a second-order polynomial. This procedure does not assume a particular functional form for $P(\Delta u)$ and works well for the tails of the probability density function when the noise has not yet grown large. The result is shown on figure 11(*a*) where we plot the normalized $\delta P = N^{1/2}(P - \widehat{P})/P^{1/2}$ as a function of Δu. In the case of Poisson statistics, the quantity δP should be distributed according to a Gaussian with unit variance. Our procedure adequately approximates the smooth part for $2 < |\Delta u/\mathrm{d}u| < 6$ and from the uniform width of the noise band in this interval we conclude that the fluctuations of the PDF are indeed that of a Poisson process. A histogram of the fluctuations for $2 < |\Delta u/du| < 6$ is shown on a logarithmic scale in figure 11(*b*). The approximate Gaussian character is evident and our assumption of a Poisson process of independent samples is further corroborated by the measured value of the standard deviation $\langle\delta P^2\rangle^{1/2} \approx 1.03$ that only slightly differs from unity.

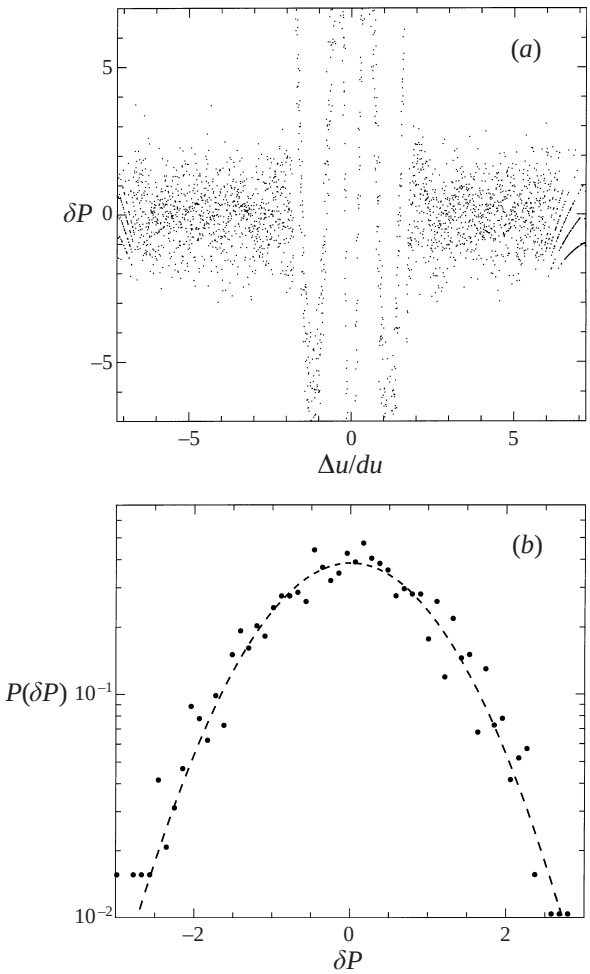

FIGURE 11. The fluctuations of a probability density function measured at separation $r/\eta = 190$ in jet turbulence (6 in table 1) using 3×10^8 samples. (*a*) The residue after subtracting the smooth part $\widehat{P}$ of the measured PDF. The determination of $\widehat{P}$ fails for $|\Delta u/du| \lesssim 2$, but works well for the tails of the PDF. (*b*) Dots: histogram of the fluctuations in the tails of the PDF in (*a*). Dashed line: Gaussian fit. The standard deviation of the measured histogram is $\langle(\delta P)^2\rangle = 1.03$.

It is now possible to derive an expression for the convergence time of high-order moments. The argument is that a moment has converged if the integrand $|(\Delta u)^p P(\Delta u)|$ has well-defined maxima. For increasing p these maxima shift to larger values of $|\Delta u|$ where the noise on a measured $P(\Delta u)$ becomes larger. At a given value of p, $p_{\max}$, it becomes impossible to decide the presence of maxima.

Let us for our present purpose assume a symmetric function $P(x)$ whose tails can be well approximated using stretched exponentials, $P(x) = a\exp\left(-\alpha x^\beta\right)$. The integrand $x^p P(x) = ax^p \exp\left(-\alpha x^\beta\right)$ reaches a maximum at

$$x_1 = \left(\frac{p}{\alpha\beta}\right)^{1/\beta}. \tag{5.5}$$

The relative Poisson noise contribution to the probability density function is $N^{-1/2}P(x)^{1/2}$. Accordingly, the noise contribution to the integrand is $N^{-1/2}x^pP(x)^{1/2} = N^{-1/2}a^{1/2}x^p\exp\left(-\alpha x^\beta/2\right)$. It reaches a maximum at

$$x_2 = \left(\frac{2p}{\alpha\beta}\right)^{1/\beta}. \tag{5.6}$$

We take the largest meaningful $p_{\max}$ as the value of p where the size of the noise contribution at x_2 equals the integrand at x_1:

$$p_{\max} \approx \tfrac{1}{2}\beta\log_2 N, \tag{5.7}$$

where N is the total number of velocity samples, and where we have assumed that $a = O(1)$. The results of figure 11 were obtained with 3×10^8 velocity samples. For this probability density function (5.7) with $\beta = 1$ predicts $p_{\max} \approx 14$, which we take as an upper limit. This value approximately agrees with that following from the fluctuations of $G_p(r)$ that were observed in repeated experimental runs, each containing 3×10^8 samples. From (5.7) it is seen that the more problematic convergence of high-order moments at small distances is due to the small value of β here. Incidentally, statistical convergence of moments $p = 20$ can only be obtained after taking a number of samples that is a factor of 4×10^3 larger (at $\beta = 1$). Peinke *et al.* (1994) also emphasize the exponential increase of N with $p_{\max}$.

6. Extrapolating high-order moments

If the tails of the probability density function can indeed be well represented by stretched exponentials, the convergence of high-order moments could be significantly improved. We will now carefully test this idea by fitting the tails of the probability density function by stretched exponentials and using this functional form to compute the contribution of the tails of $P_r(\Delta u)$ to its high-order moments. A key point is an evaluation of the goodness of fit, which is possible because the (Poissonian) nature of the fluctuations of measured PDF tails is known. In the case of perfect fits, all interesting physics would be contained in a number of velocity samples that is large enough to dependably estimate the parameters of the stretched exponentials and nothing more could be learnt from longer averages.

The computation of structure functions by stretched-exponential extrapolation was done in the following way. The contribution of left ($\Delta u \leqslant -\Delta u_0$) and right tails ($\Delta u \geqslant \Delta u_0$) of the measured probability density function to the moments was computed from the parameters of a stretched exponential fit $P(x) = a\exp\left(-\alpha|x|^\beta\right)$. The parameters a, α and β were determined from a least-squares procedure for left and right tails separately. The contribution of the central $[-\Delta u_0, \Delta u_0]$ part was computed by directly integrating the measured PDF.

Once the constants a, α and β are determined, the contribution of the tail of the PDF to the order-p moment follows simply from

$$\int_{\Delta u_0}^{\infty} ax^p\mathrm{e}^{-\alpha x^\beta}\,\mathrm{d}x = \frac{a}{\beta}\alpha^{-(p+1)/\beta}\,\Gamma\left((p+1)/\beta, \alpha(\Delta u_0)^\beta\right), \tag{6.1}$$

with the incomplete Gamma function $\Gamma(a, x)$ defined as

$$\Gamma(a, x) = \int_x^{\infty} t^{a-1}\mathrm{e}^{-t}\mathrm{d}t. \tag{6.2}$$

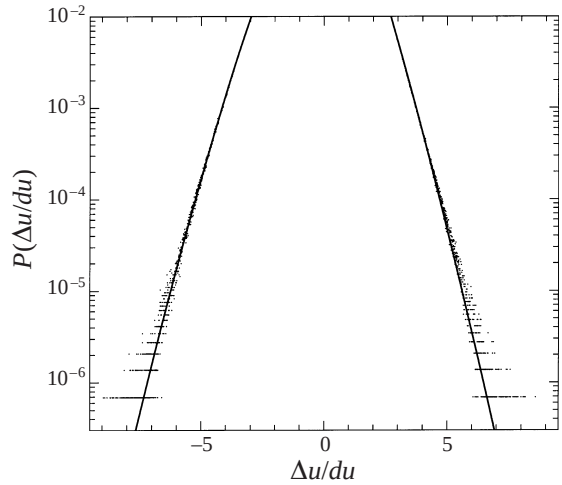

FIGURE 12. Dots: probability density function of longitudinal velocity differences in jet turbulence (6 in table 1) with $r/\eta = 190$. Full line: fit of stretched exponential $a\exp[-\alpha|\Delta u|^{\beta}]$ over $|\Delta u/du| > 1.5$. For the left side $\Delta u/du < -1.5$, $\beta = 1.37$, for the right side, $\Delta u/du > 1.5$, $\beta = 1.26$.

It must be emphasized that this extrapolation procedure cannot be a true substitute for long integration times in the experiment. The finite statistical accuracy of the tails of the PDF that results in large errors in directly determined high-order moments, now leads to errors in the parameters found for the stretched exponential. It is well known that determining the parameters of an exponential function in a least-squares fit of data with noise is an ill-conditioned problem (McWhirter & Pike 1978). This ill conditioning magnifies the noise-induced error in a, α and β. Moreover, it may well be posible that the tails of the PDF have a more complicated form than stretched exponential. We will find below that this is probably the case for the positive velocity part of longitudinal PDFs.

For the determination of the parameters of the stretched-exponential description we make explicit usage of the Poisson statistics of the tails of probability density functions. In our experiment, measured PDFs consist of events that are collected in discrete bins Δu_i. Let then n_i be the measured number of events in the bin with index i. For either the left or right tail of the PDF the parameters a, α and β follow from minimizing

$$\chi^2 = \frac{1}{M-4}\sum_{i=1}^{M}\frac{\left[n_i - a\exp(-\alpha|\Delta u_i|^{\beta})\right]^2}{n_i}, \tag{6.3}$$

where M is the number of discrete velocity bins in the part of the PDF that is parametrized. If a stretched-exponential description is adequate, the minimum of χ^2 should be $\chi^2 = 1$. An example of a stretched-exponential fit to the tails of a PDF is shown in figure 12. The dependence of χ^2 on r/η is shown in figure 13 for a total number of samples $N = 10^8$ and $N = 3 \times 10^8$. It turns out that for longitudinal measurements χ^2 is close to 1 for the negative velocity tails, which demonstrates that stretched exponentials are a good description here. For the positive Δu tails, χ^2 is larger and increases with increasing integration time of the experiment.

In these fits, the tail of the PDF was defined to be $|\Delta u| > \Delta u_0$ with $\Delta u_0/du = 1.5$ for $r/\eta \geqslant 30$ and rising to $\Delta u_0/du = 2.5$ at the smallest measured separation. Of course, better fits and smaller values of χ^2 may be obtained for larger Δu_0, but the

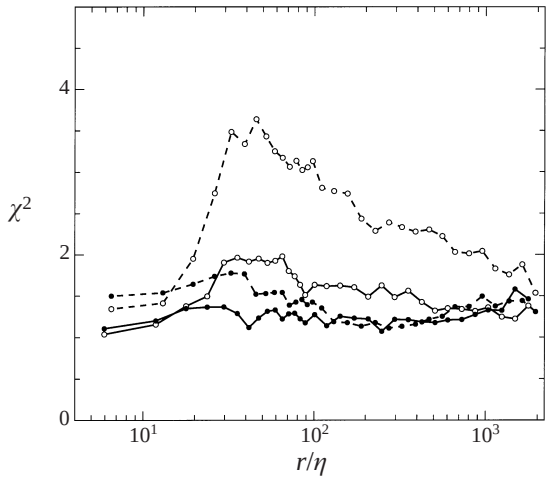

FIGURE 13. Full lines: value of χ^2 for stretched-exponential fits of PDFs for $\Delta u < -\Delta u_0$; dashed lines: χ^2 as a function of r/η for $\Delta u > \Delta u_0$. Dots: total number of samples $N = 1 \times 10^8$, open circles: $N = 3 \times 10^8$ (jet turbulence, 6 in table 1). For positive Δu the PDF appears to differ significantly from a stretched exponential.

trend of figure 13 strongly suggests that a stretched exponential description is merely approximate for $\Delta u > 0$. Transverse probability density functions are symmetric and χ^2 is always close to 1.

In figure 14 a 19th-order structure function that was computed by direct integration of measured probability density functions is compared to one that was obtained by extrapolating the tails of the same probability density functions. From this and other data it appears that for large p, the extrapolated G_p at small values of r/η is typically smaller than the directly computed G_p. At large separations, when the stretching exponent β approaches 2 and the PDFs turn Gaussian, both direct and extrapolated $G_p^L(r)$ agree well.

The extrapolated G_{19} has much less noise and now displays unambiguous scaling behaviour. The scaling behaviour of very high-order moments that are completely determined by the stretched-exponential extrapolation is caused by a highly non-trivial dependence of the parameters a, α and β on the separation r.

Although a stretched-exponential parametrization can only be approximate for the positive velocity part of longitudinal PDFs, the corresponding contribution to high-order moments is much smaller than that of the negative side of $P^L(\Delta u)$ and we expect the resulting error on the extrapolated G_{19} to be small. Obviously, the extrapolation procedure needs be reconsidered in experiments where a much larger number of velocity samples is taken and deviations from stretched-exponential behaviour for $\Delta u > 0$ become important. Noullez *et al.* (1997) have argued that, loosely, the velocity-difference PDF can never cross the single-point-velocity PDF P_u. As the latter has approximate Gaussian tails, a velocity-difference PDF with stretched exponent $\beta < 2$ will asymptotically cross P_u. Therefore, these values of β cannot hold asymptotically. We have estimated that this would occur at a number of samples that is 6 to 8 orders of magnitude larger than currently used.

The directly measured moment has oscillations that are absent in the moment that was computed using the extrapolation of the tails. We have found that these oscillations change appearance during a run, and can disappear when integrating

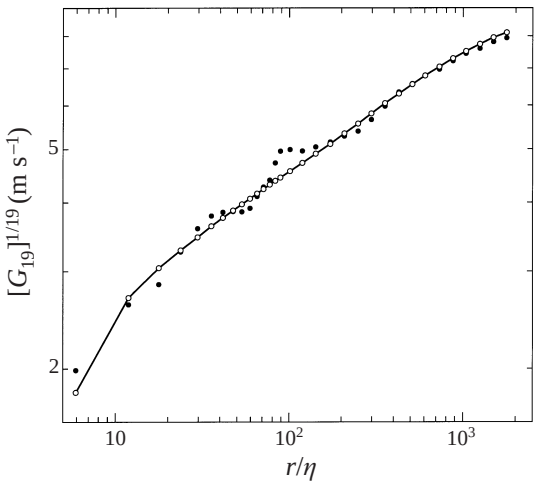

FIGURE 14. Dots: longitudinal structure function $|G_{19}(r)|^{1/19}$ as computed directly from measured PDFs; open circles $|G_{19}(r)|^{1/19}$ as computed from a stretched-exponential extrapolation from measured PDFs. After extrapolation the structure function shows clear scaling behaviour. The measured PDF is based on 3×10^8 samples. In integral scales L the integration time is $T = 2.5 \times 10^6 L/U$. (Jet turbulence, 6 in table 1.)

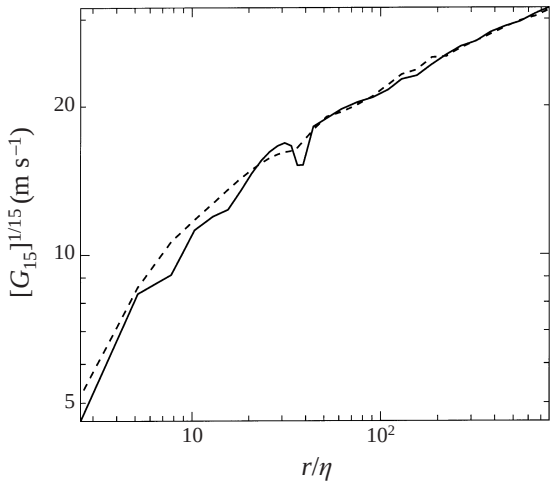

FIGURE 15. Full line: longitudinal structure function $|G_{15}(r)|^{1/15}$ as computed directly from measured PDFs that were based on 10^8 velocity samples. Dashed line: the same structure function, but after 1.5×10^9 samples. In integral scales L the latter integration time is $T = 4.7 \times 10^6 L/U$. (Experiment 1 in table 1.)

over a long time. This is illustrated in figure 15 where we show G_{15} after integrating over 10^8 and after approximately 10^9 samples. The fact that these oscillations also disappear with a better control of the statistical convergence of high-order moments through stretched-exponential extrapolation makes us strongly believe that they are due to statistical fluctuations. Similar oscillations have been noticed by Anselmet *et al.* (1984) and have been interpreted in terms of an intrinsic property of fractal sets by Smith, Fournier & Spiegel (1986). This is at variance with our interpretation. In

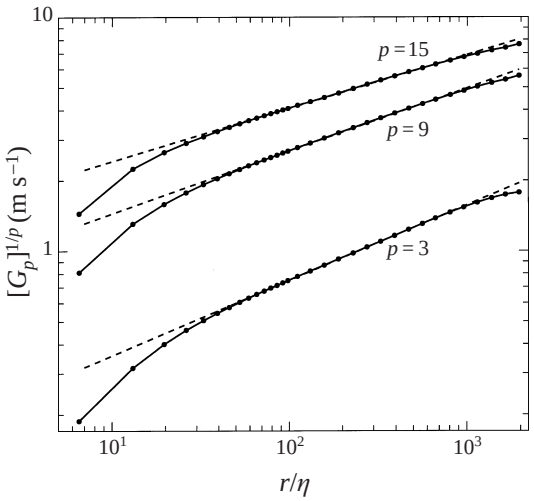

FIGURE 16. Dots: longitudinal structure functions of order 3, 9, and 15 measured in jet turbulence (6 in table 1). The total number of velocity samples N is 3×10^8 (in integral scales L the integration time is $T = 2.5 \times 10^6 L/U$). Dashed lines: fits of ideal scaling behaviour $G_p(r) \sim r^{\zeta^L(p)}$ with $\zeta^L(p)/p = 0.32, 0.27$, and 0.23, for $p = 3, 9$ and 15, respectively. The structure functions are computed by extrapolating the tails of measured PDFs using stretched exponentials.

this respect it was shown in van de Water & Schram (1989) that, even for simple model multifractal sets, such fractal oscillations almost never survive averaging.

7. Structure functions

7.1. *Longitudinal*

A central piece of information on the small-scale motion in turbulence is the structure function. We will always present it in the form $|G_p(r)|^{1/p}$, that has the dimension of velocity. Figure 16 shows a typical result for structure functions of order 3, 9, and 15 that were measured in jet turbulence. The scaling of the curves in figure 16 is indicated and the inertial range appears to be $r/\eta \in [30, 1000]$. We recall that in the case of Kolmogorov scaling, the slope of these curves would all be $1/3$. Clearly, the curves for $p > 3$ in figure 16 exhibit anomalous scaling because their slope decreases with increasing p. For the structure functions shown, the method of extrapolation of PDFs via stretched exponentials was used. Directly measured structure functions also allow the determination of scaling exponents, but the noise of the high-order moments is larger. The improvement of low-order moments ($p \leqslant 8$) through stretched-exponential extrapolation is not perceptible, but it becomes appreciable for the high-order moments.

In our experiments, an important criterion for selecting experimental configurations has been the requirement that $G_3(r)$ exhibit clear scaling behaviour which allows an unambiguous determination of the scaling exponent $\zeta(3)$. Finding the value of $\zeta(p)$ was done by fitting a straight line to $G_3(r)$ in a log-log plot and adjusting the interval $r/\eta \in [l_1, l_2]$ such as to optimize the fit. The same experimental inertial range $[l_1, l_2]$ was used in the least-squares procedure for determining $\zeta(p)$ at other values of p.

It was found that the measured values of $\zeta(3)$ differed slightly but significantly

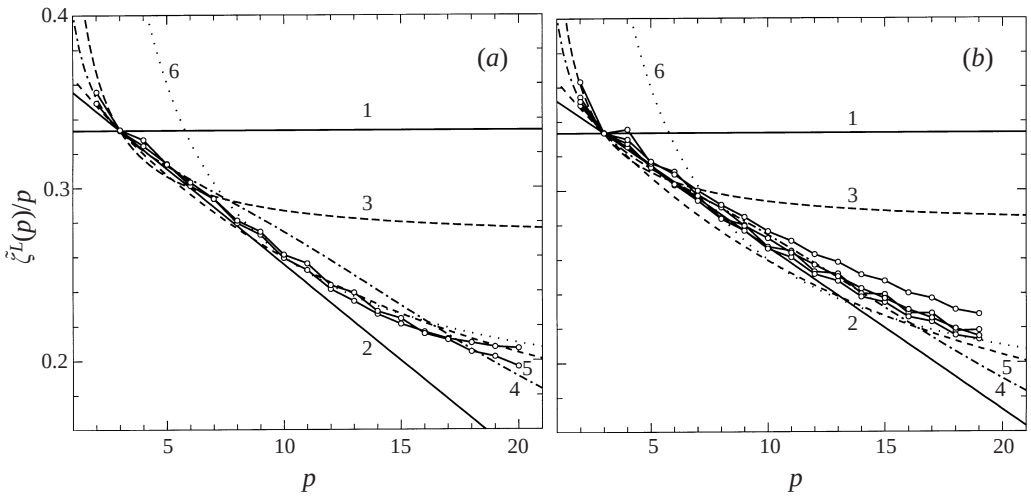

FIGURE 17. (*a*) Open circles: scaling exponents $\zeta^L(p)/p$ of longitudinal structure functions that were measured in jet and grid turbulence (2, 6 in table 1). The lines represent the prediction of several models for $\zeta(p)$. 1: Kolmogorov's prediction $\zeta(p) = p/3$; 2: Log-normal model with $\mu = 0.2$; 3: Beta model with $D = 3 - \mu = 2.8$; 4: random Beta model; 5: prediction by She & Leveque (1994); 6: prediction given by a geometric constraint of the multifractal model, $\zeta(p) = 1 + h_{\min}/p$, with $h_{\min} = 0.16$. (*b*) Open circles: scaling exponents of longitudinal structure functions. Same as (*a*), but now structure functions are computed by extrapolating the tails of the PDFs using stretched exponentials. Shown are the results of experiments in jet and grid turbulence (2, 4, 6 in table 1). The log-normal and Beta models are now computed with $\mu = 0.17$ and $D = 3 - \mu = 2.83$.

from unity (they ranged from 0.96 to 1.03). We have normalized measured $\zeta(p)$ by dividing it by $\zeta(3)$, so that the normalized $\widetilde{\zeta}(3)$ is now trivially 1.

First we have analysed experiments without extrapolating the tails of PDFs. Figure 17(*a*) shows the (normalized) scaling exponents $\widetilde{\zeta}(p)/p$ for two experiments that allowed direct measurement of $\zeta(p)$ at large p. It shows the result in a way that most clearly reveals the deviation from Kolmogorov's prediction $\zeta(p)/p = 1/3$. In order to assess the influence of the statistical convergence of measured probability density functions, we have repeated the computation of the structure functions by extrapolating the tails of the PDF using stretched exponentials. This allows the unambiguous determination of $\zeta(p)$ at large p in a larger set of experiments and the results are shown on figure 17(*b*). For low-order moments the results of the corresponding data in figures 17(*a*) and 17(*b*) agree, but for larger p the deviation from Kolmogorov scaling $\zeta(p)/p = 1/3$ becomes smaller when correcting for finite sample size statistics through stretched exponentials. The Poisson character of the statistical fluctuation of measured PDFs leads to an overestimate of the probability of the strongest events with the largest velocity differences. Because this overestimate is more severe at the small separations, where the probability density functions have wider tails, one may argue that this leads to an overestimate at the smallest separations, and thus to an overestimate of the scaling anomaly of high-order moments. This speculation seems to be supported by a comparison of figures 17(*a*) and 17(*b*).

In figure 17 it is seen that $\widetilde{\zeta}^L(p)$ for $p = 2, 3, 4$ (and 5) does not follow a smooth curve and displays an apparent asymmetry between even and odd exponents. Let us for convenience define $A_\zeta(p) = [\zeta^L(p-1) + \zeta^L(p+1)]/2 - \zeta^L(p)$ as a measure for this asymmetry. In § 2 it was argued that the existence of a substantial $A_\zeta(3)$ would be

caused by forcing effects that are difficult to avoid in laboratory turbulent flows. We do not believe that the asymmetry $A_\zeta(3)$ in figure 17 is due to this finite-size effect as we have found slightly different values of $A_\zeta(3)$, even in repetitions of the same experiment under slightly different conditions. We conjecture that this difference is due to slightly different dynamic characteristics of the hot-wire probe that are not completely understood. In fact, the data that were selected in figure 17(*a*) have the smallest asymmetry $A_\zeta(3)$ between odd and even exponents.

In other experiments in a turbulent boundary layer at low Re_λ ($Re_\lambda < 200$) that are not further discussed here, the asymmetry persists for large p and the structure functions strongly violate the approximate similarity $[G_2(r)]^{1/\zeta(2)} \sim |G_3(r)|$ (which is used in 'extended self-similarity'). The results of this experiment are in complete agreement with a similar experiment that was analysed by Stolovitsky *et al.* (1993). The asymmetry that is seen in this case appears to be genuine and might be caused by the finite-size effect discussed in § 2. However, it must also be noted that the flow in this case is highly anisotropic, with the longitudinal integral length scale approximately a factor of three larger than the distance to the boundary.

On figure 17 we show scaling exponents $\widetilde{\zeta}^L(p)$ up to order $p = 20$. As stated above, the exponents for $p \gtrsim 14$ are either from very small statistical samples of very large velocity differences (figure 17*a*) or are determined from an extrapolation of the probability density function towards large velocity differences (figure 17*b*). Fully converged moments at $p \approx 20$ are simply unattainable in a practical experiment.

The intermittency factor $\mu \equiv 2 - \zeta^L(6)$ plays a central role in the statistical study of turbulent fluctuations. It is the only parameter in the log-normal model (2.3) and it is also the scaling exponent of dissipation correlations. From figure 17(*a*) we deduce (from normalized ζ_p) $\widetilde{\mu} = 0.20$, whereas from figure 17(*b*) we conclude $\widetilde{\mu} = 0.17 \pm 0.02$. As expected, μ decreases when correcting for the finite sample size. Let us emphasize that the quoted uncertainty reflects the measured variation of μ in different experiments; the variation in repeated runs of the same experiment is much smaller.

Obviously, the data of figures 17(*a*) and 17(*b*) show a consistent and significant deviation from the Kolmogorov (1941) prediction. In § 2 several intermittency models were discussed that predict the scaling exponent $\zeta(p)$. The question now is if our data can discriminate between these intermittency models. From figure 17 it appears that the simple Beta model, that predicts a linear $\zeta(p)$, is incorrect. Clearly, the structure of the turbulent velocity field is more complex for a simple fractal with a single dimension to be an adequate description. According to (2.3), the log-normal model predicts the graph of $\zeta(p)/p$ to be a straight line that passes through the points $p = 3, \zeta(3)$ and $p = 6, \zeta(6)$. Our data deviate from this linear behaviour only at rather large values of p ($p \gtrsim 10$). Still, we believe that this deviation is significant. The other multifractal models, in particular the one by She & Leveque (1994), follow our data closely, although discrepancies are evident. Surprisingly, in this model it is assumed that the strongest singularities are on lines, for which a line measurement in three dimensions corresponds to a negative dimension of the intersection set. In the case of a limiting single singularity strength $h_{\min}$ with $D_s(h_{\min}) = -2 + D(h_{\min}) = 0$, the multifractal model predicts a large-p behaviour of the scaling exponent $\zeta^L(p)$ according to (2.11). This prediction is shown for $h_{\min} = 0.16$. The data appear to favour this behaviour above the linear dependence on p of $\zeta^L(p)/p$ of the log-normal model. Much of the scatter in the measured $\widetilde{\zeta}(p)$ is due to the asymmetry between even and odd exponents. Of course, this problem vanishes if moments of absolute-value velocity differences $|\Delta u|$ are considered. These results, not shown here, confirm our

conclusions. Incidentally, the models discussed are scaling models and would equally apply to moments of $|\Delta u|$; still we prefer comparison with the proper moments.

We conclude that the scaling exponent $\widetilde{\zeta}^L(p)$ differs very significantly from Kolmogorov's prediction $\zeta^L(p) = p/3$. This scaling anomaly of turbulent velocity fluctuations appears to be a genuine property of fully developed turbulence. Figure 17 is a central result of this paper. It shows the consistency of the scaling exponent $\widetilde{\zeta}^L(p)$ in a range of experiments that were done in a variety of turbulent flows. Most notably, the conditions for application of Taylor's hypothesis vary as u/U ranges from $u/U = 0.05$ to $u/U = 0.18$. Except at the largest values of p, much of the variation of $\zeta^L(p)$ is a systematic variation. The scaling exponent depends on the details of the experiment in a way that we do not understand completely. The experimental evidence for intermittency and scaling anomaly has recently been questioned by Grossmann *et al.* (1994) and attributed to finite-size effects and the presence of shear. The data presented in figure 17(*b*), where a consistent anomaly is found for different flows, are in clear disagreement with this suggestion.

The precision with which $\zeta(p)$ it can be measured in experiments, however, limits our ability to discriminate between simple models that are based on quite different grounds. A clear need arises to test other predictions of these models.

7.2. *Multiscaling*

One of these predictions concerns the precise functional form of the structure function. The multiscaling property of multifractals leads to a prediction of the behaviour of structure functions at separations r where viscosity is important. As explained in § 2 the consequence of multiscaling is that the scaling of G_p extends deeper into the viscous subrange as p becomes larger. That this is actually the case may already be discerned from figure 16 but we would like to quantify this effect more precisely.

Following the suggestion by Benzi *et al.* (1993) we write the structure function as $G_p(r) = (f_p(r)r)^{\zeta(p)}$. The function $f_p(r)$ gauges the deviation from ideal scaling behaviour, $G_p(r) \simeq r^{\zeta(p)}$. As argued above, the multiscaling hypothesis predicts that this deviation in the intermediate viscous range will be smaller for larger moments p. For the moment we assume intermediate viscous scales to be $\eta \lesssim r \lesssim 30\eta$. In order to highlight the p-dependence of $f_p(r)$ we define the residual function $g_p(r) \equiv f_p(r)/f_2(r)$. Roughly, the behaviour of the function $g_p(r)$ for $p > 2$ will be as follows: (i) at very small scales, $r \approx \eta$, the velocity field is smooth and $G_p(r) \simeq r^p$. Therefore, $g_p(r) \simeq r^{\gamma(p)}$, with a positive exponent $\gamma(p) = p/\zeta(p) - 2/\zeta(2)$. (ii) In the intermediate viscous range the multiscaling hypothesis predicts $g_p(r) > 1$. (iii) For inertial-range scales, $30\eta \lesssim r \lesssim L$, the (properly normalized) function $g_p(r)$ is unity because all scaling behaviour has been captured in the exponent $\zeta(p)$. Summarizing, for r decreasing from $r \approx L$, the function g_p is first constant, then increases and reaches a maximum at intermediate viscous scales, and decreases again when r becomes $O(\eta)$. According to the multiscaling hypothesis, the steepness of the rise of g_p increases with increasing order p. The actual height of the maximum is controlled by unknown factors.

Figure 18 shows the function $g_p(r)$ on a log–log scale for various experiments. The Taylor microscale Reynolds numbers in these experiments ranged from $Re_\lambda = 3 \times 10^2$ to 8×10^2. The small Re_λ experiments, in particular, have a small inertial range where $g_p(r)$ is flat. The spread of the measured $g_p(r)$ at large scales is not due to statistical error but reflects the different experimental conditions of table 1. The results shown in figure 18 were obtained without using the stretched-exponential extrapolation of PDF's. Using this extrapolation gives very similar results.

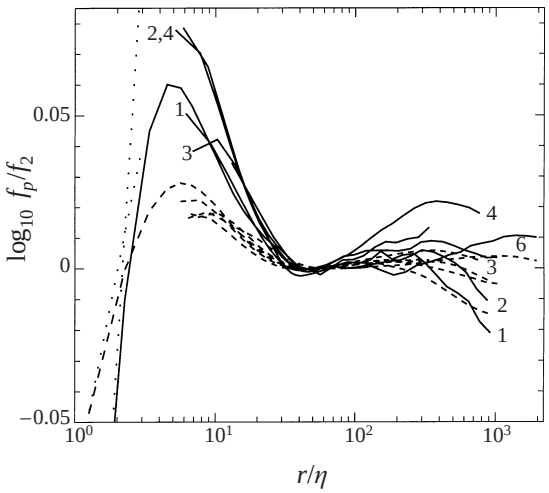

FIGURE 18. Residual function $g_p(r)$ for $p = 4$ (dashed lines) and $p = 8$ (full lines) in a variety of turbulent flows. The numbers are flow conditions in table 1. Experiment 1 was repeated at a large enough sampling rate to resolve $r \approx 2\eta$. The predicted small-r scaling behaviour of this experiment, $g_p(r) \sim r^{\gamma(p)}$ is shown by the dotted lines.

The p-dependence of g_p is precisely as predicted by the multiscaling hypothesis. For the curves in figure 18 with the filter set at 10 kHz the temporal resolution is not fine enough to observe the predicted maximum of $g_p(r)$. One of the experiments was also done at a large enough sampling rate (45 kHz) to resolve $r \approx 2\eta$. The corresponding curves clearly show the maximum and agree with the predicted small-r scaling, $g_p(r) \sim r^{\gamma(p)}$.

7.3. *Transverse*

Figure 19 shows transverse structure functions $G_p^T(r)$ of order $p = 3, 9$ and 15. The odd orders are defined as $G_p^T(r) = \langle |\Delta u|^p \rangle$. Transverse probability density functions are symmetric and these odd orders merely provide a convenient interpolation between adjacent even orders. The statistical convergence of high-order moments was improved by fitting stretched exponentials to the tails of measured PDFs. The transverse structure functions also show clear evidence of scaling anomaly. Here we have again found that $\zeta(3)$ deviates significantly from 1. The scaling exponents $\widetilde{\zeta}^T(p)$ for two experiments in grid turbulence are shown in figure 20. As in the longitudinal case, they have been normalized by dividing them with the measured $\zeta^T(3) = 1.08$. We have also determined the scaling exponents directly from measured PDFs, without using the stretched-exponential extrapolation of the tails; the difference with the exponents based on extrapolated PDF tails is only slight. Taking moments of absolute-value velocity differences allows the computation of orders $p \leqslant 1$. The associated scaling exponents are also shown in figure 19 where $\zeta(p)/p$ for $p = 0$ is defined as the scaling of $\exp(\langle \log |\Delta u| \rangle)$. The exponents for $p \leqslant 1$ are also strongly anomalous. They significantly disagree with the predictions of both the simple Beta and the random Beta model, but agree with the log-normal model and the model by She & Leveque (1994).

Comparison of the transverse results to the longitudinal scaling exponents in figure 17 shows that for $p \gtrsim 5$ the deviation from $\zeta^T(p)/p = 1/3$ is significantly larger. In the language of the multifractal model this implies that the transverse

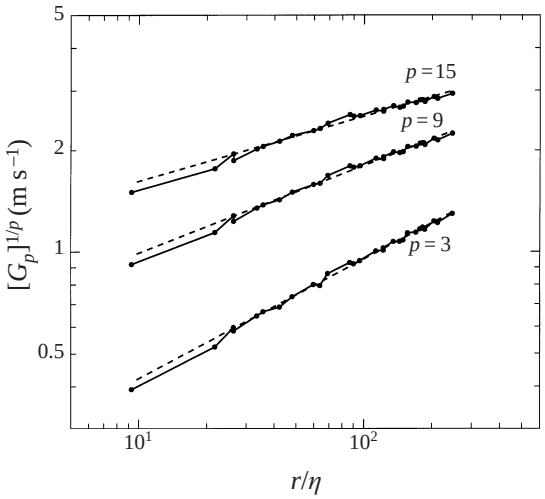

FIGURE 19. Dots: transverse structure functions of order 3, 9, and 15 measured in grid turbulence (5 in table 1). The total number of velocity samples N is 1×10^8. Dashed lines: fits of ideal scaling behaviour $G_p(r) \sim r^{\zeta(p)}$ with $\zeta(p)/p = 0.35, 0.26$, and 0.19, for $p = 3, 9$. and 15, respectively. Because transverse probability density functions are symmetric, these odd-order structure functions are defined as $G_p^T(r) = \langle |\Delta u|^p \rangle$.

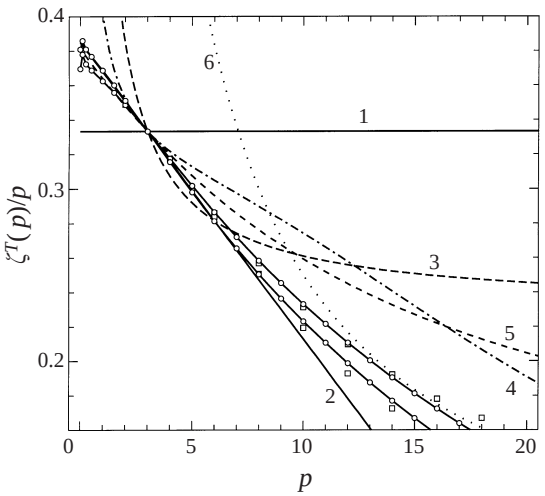

FIGURE 20. Scaling exponents $\zeta^T(p)/p$ of transverse structure functions that were measured in grid turbulence (5 in table 1). Open circles connected by lines: using a stretched-exponential extrapolation of the tails of probability density functions; open squares: using measured PDFs only. The lines represent the prediction of several intermittency models, that are detailed in the caption of figure 17. The log-normal and Beta models are computed with $\mu = 0.30$ and $D = 3 - \mu = 2.70$. The geometric constraint of the multifractal model is now $\zeta(p) = 2 + h_{\min}/p$, with $h_{\min} = 0.05$.

scaling exponents are determined by stronger singularities. The difference with the longitudinal exponents now also shows in a marked discrepancy with the model by She & Leveque (1994) and the random Beta model. We finally recall that, contrary to the longitudinal case, measurement of the transverse structure functions does not rely on Taylor's hypothesis.

8. Conclusion

In this paper we have given firm evidence for the anomaly of scaling exponents $\widetilde{\zeta}^L(p)$, and have given initial results for the transverse scaling exponent $\widetilde{\zeta}^T(p)$. By concentrating on the statistical convergence of high-order structure functions, both by using new instrumentation and by careful extrapolation of PDFs, we have been able to give precise values for $\widetilde{\zeta}^L(p)$ that do not appear to depend on the particular experimental configuration.

The transverse scaling exponent $\widetilde{\zeta}^T(p)$ deviates more strongly from the Kolmogorov (1941) result than the longitudinal scaling exponent. Several interesting speculations about the meaning of this result are possible. The first one is that the stronger anomaly of $\widetilde{\zeta}^T(p)$ is due to anisotropy of the flow. However, the longitudinal scaling exponent $\widetilde{\zeta}^L(p)$ of the same flow arrangement agrees with that of other flow geometries (see for example figure 17*b*). If the strongest singularities in turbulence exist on lines, a heuristic explanation of the stronger transverse anomaly would be that the chances of intersecting these in a planar (transverse) setup are bigger than in the longitudinal one. Noullez *et al.* (1997) give a quantitative argument illustrating the greater ease of detecting a slender vortex filament in a transverse setup.

An intriguing question is whether new physics will emerge when using ever longer integration times that allow the measurement of ever larger-order moments. The answer to this question lies in the asymptotic form of the scaling exponent $\zeta(p)$ for large p. Integration times do not need to be longer than necessary for establishing this asymptotic form. It would be interesting to study the fluctuations in high-order moments. If those are determined by the geometry of intersecting fractal sets, the appropriate framework would be the theory of large deviations (Mandelbrot 1990).

We believe that experiments on the small-scale structure of turbulence should exploit different geometric arrangements for measuring velocity statistics. A program of these experiments (with new ways of real-time data processing) is currently underway in our laboratory. In the present work we have emphasized instrumentation aspects and we have found that highly non-trivial questions remain, for example concerning the precise understanding of probes that can be used to accurately measure small-scale motion.

We have not touched upon the scaling with Reynolds number. In our experiments it could at most be varied by a factor of two to four. At small values ($Re_\lambda \approx 200$) a scaling inertial range is absent and scaling exponents could not be determined dependably. On the other hand, the largest Re_λ is restricted by the finite size of the laboratory experiment. In conventional laboratory experiments it may be possible to push the largest Re_λ to 2000, in which case the Reynolds number can be varied by one order of magnitude. A large range of Reynolds numbers has been be accessed by Chabaud *et al.* (1994) and Maurer, Tabeling & Zocchi (1994) in laboratory-scale experiments employing helium gas at cryogenic temperatures. Because the Kolmogorov length is $O(\mu\mathrm{m})$, the instrumentation of these experiments is still difficult. The advantage of laboratory turbulence experiments in air is that instrumentation development (such as for measuring transverse velocity differences) is well feasible. A very significant step forward would be the combination of these two approaches in a single experiment.

Essential contributions to this work have been by Jan Niessen and Gerard Trines who have designed and built the computer controlled anemometers, and by Rob van der Berg, who has manufactured numerous hot- wire probes. This work is also part of the 'Stichting voor Fundamenteel Onderzoek der Materie (FOM)', which is finan-

cially supported by the 'Nederlandse Organisatie voor Wetenschappelijk Onderzoek (NWO)'.

REFERENCES

Anselmet, F., Gagne, Y., Hopfinger, E. J. & Antonia, R. A. 1984 *J. Fluid Mech.* **140**, 63–89.

Antonia, R. A., Phan-Tien, N. & Chambers, J. A. 1980 *J. Fluid Mech.* **100**, 193–208.

Antonia, R. A., Chambers, J. A. & Browne, L. W. B. 1983 *Exps. Fluids* **1**, 213–219.

Benzi, R., Biferale, L., Paladin, G., Vulpiani, A. & Vergassola, M. 1991 *Phys. Rev. Lett.* **67**, 2299–2302.

Benzi, R., Paladin, G., Parisi, G. & Vulpiani, A. 1984 *J. Phys.* A: *Math. Gen.* **17**, 3521–3531.

Benzi, R., Ciliberto, S., Tripiccione, R., Baudet, C., Massaioli, F. & Succi, S. 1993 *Phys. Rev.* E. **48** , R29–R32.

Bremhorst, K. & Gilmore, D. B. 1976 *J. Phys.* E: *Sci. Instrum.* **9**, 1097–1100.

Camussi, R., Barbagallo, D., Guj, G. & Stella, F. 1996 *Phys. Fluids* **8**, 1181–1191.

Castaing, B., Gagne, Y. & Hopfinger, E. J. 1990 *Physica* D **46**, 177–200.

Chavarria, G. R., Baudet, C. & Ciliberto, S. 1995 *Phys. Rev. Lett.* **74**, 1986–1989.

Chhabra, A. B., Meneveau, C., Jensen, R. V. & Sreenivasan, K. R. 1989 *Phys. Rev.* A **40**, 5284–5294.

Chhabra, A. B. & Sreenivasan, K. R. 1991 *Phys. Rev.* A **43**, 1114–1117.

Chhabra, A. B. & Sreenivasan, K. R. 1992 *Phys. Rev. Lett.* **68**, 2762–2765.

Chabaud, B., Naert, A., Peinke, J., Chilla, F., Castaing, B. & Hébral, B. 1994 *Phys. Rev. Lett.* **73**, 3227–3231.

Comte-Bellot, G. & Corrsin, S. 1966 *J. Fluid Mech.* **25**, 657–682.

Frisch, U. 1995 *Turbulence; The Legacy of A. N. Kolmogorov*. Cambridge University Press.

Frisch, U., Sulem, P.-L. & Nelkin, M. 1978 *J. Fluid Mech.* **87**, 719–736.

Frisch, U. & Vergassola, M. 1991 *Eur. Phys. Lett.* **14**, 439–444.

Grossmann, S., Lohse, D., L'Vov, V. & Proccacia, I. 1994 *Phys. Rev. Lett.* **73**, 432–435.

Halsey, T. C., Jensen, M. H., Kadanoff, L. P., Procaccia, I. & Sraiman, B. I. 1986 *Phys. Rev.* A **33**, 1141–1151.

Herweijer, J. A., Nijmweegen, F. C. van, Kopinga, K., Voskamp, J. H. & Water, W. van de. 1994 *Rev. Sci. Instrum.* **65**, 1786–1787.

Jensen, M. H., Paladin, G. & Vulpiani, A. 1991 *Phys. Rev. Lett.* **67**, 208–211.

Kailasnath, P., Sreenivasan, K. R. & Stolovitsky, G. 1992 *Phys. Rev. Lett.* **68**, 2766–2769.

Kolmogorov, A. N. 1941 *Dokl. Akad. Nauk.* **26**, 115. (Reprinted in *Proc. R. Soc. Lond.* A **434**, 9–13 (1991).)

Kolmogorov, A. N. 1962 *J. Fluid Mech.* **13**, 82–85.

Kuznetsov, V. R., Praskovsky, A. A. & Sabelnikov, V. A. 1992 *J. Fluid Mech.* **243** 595–622.

Mandelbrot, B. B. 1974 *J. Fluid Mech.* **62**, 331–358.

Mandelbrot, B. B. 1990 *Physica* A **163**, 306–315.

Maurer, J., Tabeling, P. & Zocchi, G. 1994 *Europhys. Lett.* **26**, 31–36.

McWhirter, J. G. & Pike, E. R. 1978 *J. Phys.* A **11** 1729–1745.

Meneveau, C. & Sreenivasan, K. R. 1987 *Phys. Rev. Lett.* **59**, 1424–1427.

Meneveau, C. & Sreenivasan, K. R. 1991 *J. Fluid Mech.* **224**, 429–484.

Molenaar, J., Herweijer, J. A. & Water, W. van de 1995 *Phys. Rev.* E **52**, 496–509.

Monin, A. S. & Yaglom, A. M. 1975 *Statistical Fluid Mechanics*, Vol. II. (MIT Press).

Noullez, A., Wallace, G., Lempert, W., Miles, R. B. & Frisch, U. 1997 *J. Fluid Mech.* **339**, 287–307.

Paladin, G. & Vulpiani, A. 1987 *Phys. Rev.* A **35**, 1971–1973.

Parisi, G. & Frisch, U. 1985 *Proc. Intl School in Physics, 'E. Fermi', Course LXXXVIII* (ed. M. Ghil, R. Benzi & G. Parisi), p. 84. North Holland.

Peinke, J., Castaing, B., Chabaud, B., Chillà, F., Hébral, B. & Naert, A. 1994 *Fractals in the Natural and Applied Sciences (A-41)* (ed. M. M. Novak). Elsevier.

Saddoughi, S. G. & Veeravalli, S. V. 1994 *J. Fluid Mech.* **268**, 333–372.

She, Z.-S. & Leveque, E. 1994 *Phys. Rev. Lett.* **72**, 336–339.

Sirovich, L., Smith, L. & Yakhot, V. 1994 *Phys. Rev. Lett.* **72**, 344–347.
Smith, L. A., Fournier, J. D. & Spiegel, E. A. 1986 *Phys. Lett.* A **114**, 465–468.
Sreenivasan, K. R. & Meneveau, C. 1988 *Phys. Rev.* A **38**, 6287–6295.
Stolovitzky, G., Kailasnath, P. & Sreenivasan, K. R. 1992 *Phys. Rev. Lett.* **69**, 1178–1181.
Stolovitzky, G., Sreenivasan, K. R. & Juneja, A. 1993 *Phys. Rev.* E **48**, R3217–R3220.
Tennekes, H. & Lumley, J. L. 1972 *A First Course in Turbulence.* MIT press.
Vainshtein, S. I. & Sreenivasan, K. R. 1994 *Phys. Rev. Lett.* **73** 3085–3088.
Water, W. van de & Herweijer, J. A. 1995 *Phys. Rev.* E **51**, 2669–2671.
Water, W. van de & Schram, P. P. J. M. 1989 *Phys. Lett.* **140A**, 173–178.
Vassilicos, J. C. 1992 *Topological Aspects of the Dynamics of Fluids and Plasmas* (ed. H. K. Moffatt, G. M. Zaslavsky, P. Comte & M. Tabor). Kluwer.
Wu, X.-Z., Kadanoff, L., Libchaber, A. & Sano, M. 1990 *Phys. Rev. Lett.* **64**, 2140–2143.
Yakhot, V. 1995 Corrections to scaling in strong turbulence. Unpublished.
Zocchi, G., Tabeling, P., Maurer, J. & Williame, H. 1994 *Phys. Rev.* E **50**, 3693–3700.